Elevated temperature fatally disrupts nuclear divisions in the early *Drosophila* embryo.

Girish Kale[1,2,*], Pratika Agarwal[1], J Jaime Diaz-Larrosa[1], Steffen Lemke[1,2,*]

[1] Centre for Organismal Studies, University of Heidelberg, Heidelberg. Germany
[2] Institute of Biology, University of Hohenheim, Stuttgart, Germany
* Correspondence: G.K. (girish.kale@uni-hohenheim.de), S.L. (steffen.lemke@uni-hohenheim.de)

Abstract:

Temperature variations can challenge animal survival, with elevated temperatures presenting distinct vulnerabilities at different stages of the animal life cycle. Embryonic development is known to be especially vulnerable, though the molecular mechanisms that underlie this vulnerability remain unclear. Here we investigate how elevated temperature affects embryogenesis in *Drosophila melanogaster*, an insect model known for extensively characterized genetic makeup and developmental processes.

We identify the first three hours as a critical window in which *Drosophila* embryos are particularly vulnerable to elevated temperature. This period includes the formation of a syncytial blastoderm, which involves 4 rounds of meta-synchronous nuclear divisions at the embryonic cortex, and cellularization that leads to the formation of the cellular blastoderm. Embryos exposed to elevated temperature during this period subsequently exhibited developmental defects at the gastrulation stage, leading to increased lethality. At elevated temperature, we observed an increase in mitotic failures causing a loss of cortical nuclei during cellularization. There is also a local crowding of nuclei and an increase in asynchrony between the nuclear cycles in the center vs. the poles. Interestingly, these features cooperatively amplify the frequency of mitotic failures, leading to holes in the blastoderm epithelium.

Further mechanistic analysis of mitotic failures revealed that they trigger DNA damage response. Focusing on cell biological causes of mitotic failures, we found that the interaction between F-actin and microtubules is weakened at elevated temperature. We performed functional tests to determine whether known regulators of mitosis could rescue mitotic failures, blastoderm hole formation, and improve embryo survival. We further analyzed genomic datasets from wild populations to determine whether these regulators also carry signatures of adaptation in wild populations.

Our genetic rescue experiments show that in *Drosophila* embryos, the interaction between cortical F-actin and astral microtubules of mitotic spindle is vulnerable to disruption at elevated temperatures, leading to mitotic failures that can be potentially rescued by modulating the expression of just a few factors. We propose that levels of expression of corresponding genes could be used as indicators to predict the effects of increasing temperature variations on insect populations.

Keywords:

Blastoderm formation, elevated temperature, microtubule - F-actin interaction, nuclear division defects, embryo lethality, genetic rescue, *Drosophila*

Introduction:

It has been suggested that the current rise in average global temperatures and the amplitude of temperature fluctuations can affect species fitness and result in a loss of biodiversity[1]. It is unclear whether effects on species fitness are direct consequences of the temperature rise, particularly since many species are likely experiencing a rather gradual departure from optimal conditions of temperature, which have previously evolved in a species-specific manner. Previous studies suggest that, under some circumstances, even such gradual departures could affect animal survival. For instance, studies have shown that a gradual departure from normal temperatures, e.g., experienced by fevers during pregnancy produce birth defects in humans[2–4], indicating that temperature conditions tolerable by an adult may be more detrimental to the embryo. This raises the possibility that specific aspects of embryo development are more vulnerable to temperature increase. Consistent with this notion, previous studies in model organisms have shown that temperature is a key factor that determines the fidelity of embryonic development; rat and zebrafish embryos show an increase in developmental defects at elevated temperatures[5–8]. Yet the mechanisms underlying vulnerability in embryonic development at elevated temperatures remain unclear. Here we explore whether exposure to elevated temperature is detrimental to embryonic development in the insect model *Drosophila melanogaster* (henceforth, *Drosophila*), and examine the consequences in terms of population-level parameters such as embryo survival.

In nature, animals rarely experience highly steady temperatures, but they do experience a range of temperatures to which they are generally well adapted. Increasing temperatures accelerate diverse physiological processes, including development, growth, and regeneration, making the timing of events temperature-dependent[9]. Developmental processes can be viewed as networks of biochemical reactions occurring simultaneously or in rapid succession. The Arrhenius equation, long used to describe the temperature dependence of biochemical reactions, has more recently been applied to capture the effects of temperature on the rate of physiological processes, particularly during embryonic development[10,11]. However, in contrast to chemical reactions *in vitro*, where temperatures often exceed physiological ranges, complex biological processes *in vivo* – such as embryonic development – follow the Arrhenius equation, provided that temperatures remain within the relatively narrow range typically experienced by the organism. With a transition from 28°C to 30°C, *Drosophila* no longer exhibit an acceleration of embryonic development[10–12], suggesting that 29°C marks a threshold at which elevated temperatures challenge development and exceeds the physiological range over which the Arrhenius equation accurately describes developmental rates, while lower temperatures remain effectively normal. To test this hypothesis, we analyzed the fidelity of development at an elevated temperature of 29°C, compared with controls at the normal culture temperature of 25°C.

Previous studies have found that *Drosophila* embryo development beyond the first 4-6 hours is robust to even acute exposure to high temperatures[13], suggesting that potential embryonic vulnerabilities are likely to occur and be observed during the first few hours of development. *Drosophila* embryo development starts with fertilization and egg deposition. Following fertilization, the embryo undergoes nine rounds of syncytial nuclear divisions within the yolk. Following these divisions, most nuclei are anchored to the periphery of the embryo, where four more rounds of nuclear division take place during a stage called syncytial blastoderm[14]. These divisions are facilitated by pseudo-cleavage furrows, i.e., temporary membrane invaginations that resemble a half-cell and slowly form around the nuclei during interphase-metaphase. They are subsequently reabsorbed into the embryo cortex rapidly during anaphase-telophase[15]. Following a total of 13 nuclear divisions, the resulting ~6000 nuclei simultaneously segregate into individual cells and produce the blastoderm epithelium in a process called cellularization[16]. This occurs at about 3 hrs from fertilization. It marks the beginning of gastrulation, which involves changes in cell shape[17], rearrangements of cell contacts[18],

82 and further rounds of cell divisions in isolated mitotic domains[19]. All of these events facilitate early
83 morphogenesis.

84 In our experiments, we found that exposing embryos to 29°C during the first 3 hours of embryonic
85 development leads to a significant increase in population-level embryonic lethality during the gastrulation
86 stage. Examinations at the cell and tissue level revealed mitotic failures, which lead to the loss of nuclei during
87 the syncytial blastoderm and especially the cellularization stage. Additionally, embryos developing at 29°C
88 showed nuclear crowding in the central region of the embryo and greater asynchrony of nuclear division
89 cycles between the central regions and at the poles. We show that nuclear crowding and nuclear cycle
90 asynchrony combine to increase the local propensity of mitotic failures. Local clusters of mitotic failures lead
91 to regions devoid of nuclei/cells ('holes'), which disrupts the continuity of the blastoderm as primary
92 epithelial tissue. The molecular dissection of mitotic failures in the blastoderm revealed that they trigger a
93 DNA damage response, which mitotically arrests the defective daughter nuclei, resulting in their expulsion
94 from the embryo cortex. We show that cytoskeletal elements, F-actin and microtubules, show incongruent
95 dynamics at 29°C, suggesting a weakening of their interaction during mitosis, implicating mitotic failures at
96 the core of developmental vulnerabilities at elevated temperature. In an attempt to enhance the resilience
97 of nuclear divisions at 29°C and rescue temperature-induced developmental defects, we overexpressed
98 specific genes that regulate cell polarity, microtubule-F-actin interactions, and mitotic spindle orientation.
99 Our results suggest a genetically rescuable vulnerability in microtubule-F-actin interactions during nuclear
100 divisions at elevated temperatures. Notably, the genes we identified as capable of providing a genetic rescue
101 to temperature-induced developmental defects could be recovered in a genome-wide analyses of data on
102 genetic variation in natural populations along temperature clines. In summary, our work identifies cell
103 biological defects caused by elevated temperatures and links them to population-level lethality and fitness.
104 This offers insights into the broader implications of vulnerability to elevated temperatures during a defined
105 time span in the life history of flies and provides an initial handle to quantitatively and mechanistically predict
106 embryo fitness at elevated temperature.

107 **Results:**

108 **Early exposure to elevated temperature reduces embryo survival due to gastrulation defects**

109 To explore how elevated temperature affects the early development of *Drosophila* embryos, we exposed
110 young embryos to 29°C and asked how many of them survived and how they developed. To investigate
111 alterations in the rate of embryos hatching into larvae, we first differentiated the effects of temperature
112 exposure by timing: from the moment of deposition until just before gastrulation begins (~3 hours), and
113 during a similar time starting from gastrulation onset (refer to Figure 1A for experimental temperature
114 regimen). In both scenarios, we observed a notable increase in embryonic lethality (Figure 1B), pinpointing a
115 critical vulnerability especially during the pre-gastrulation phase of development. This finding was
116 unexpected, as prior research suggested that the genetic mechanisms governing embryonic patterning
117 during this phase were resilient to temperature fluctuation[20,21], indicating a more systemic effect, possibly
118 rooted in cell biology.

119 To address when and how embryos died after early exposure to 29°C, we maintained embryos until late
120 cellularization stage at 29°C and then recorded their development using confocal microscopy time-lapse
121 imaging at 25°C. Embryonic development in these recordings was analyzed qualitatively as well as
122 quantitatively. Qualitatively, many embryos displayed moderate anomalies during gastrulation, including
123 twisting along the embryo's anterior-posterior axis (Figure 1C-D), exemplifying transient defects in the
124 bilateral symmetry of embryonic development. Notably, these twisted embryos seemed to recover from their
125 defects and continued to develop. By contrast, a minority of embryos exhibited severe gastrulation defects,

126 culminating in developmental cessation and lethality (Figure 1E). Quantitatively, surviving embryos after
127 exposure to 29°C did not differ statistically significantly from those after control exposure to 25°C, neither in
128 the rate of germband extension (GBE, Figure 1F) nor in the timing of other key developmental milestones
129 (Figure 1G). Overall, this suggests that if embryos surpass the gastrulation stage, they proceed without
130 detectable developmental delays.

131 Taken together, our findings underline increased embryonic lethality during gastrulation due to prior
132 exposure to 29°C, highlighting the detrimental effects of elevated temperature. Previous work has
133 demonstrated that genetic patterning is robust to temperature perturbations[20,21], suggesting that the
134 observed defects are unlikely to be directly caused by a failure of embryonic patterning per se. To explain the
135 observed fatal defects during gastrulation stage, we instead hypothesized that nuclei, who ultimately
136 interpret embryonic patterning information into cell and tissue movements, might have exhibited fatal
137 defects in their dynamic behavior during blastoderm formation. To address this possibility, we investigated
138 nuclear dynamics during pre-gastrulation development.

139 **A clustered loss of nuclei at elevated temperature likely causes gastrulation defects and embryo lethality**

140 Pre-gastrulation development in flies and other insects involves nuclei dividing deep within the yolk before
141 their arrival at embryo's cortex, where they must be securely anchored while undergoing further rounds of
142 division. Ultimately, the tight and even cortical distribution of those syncytial nuclei is crucial for the
143 generation of blastoderm epithelium and its subsequent morphological changes during gastrulation.

144 To address whether defects during gastrulation could stem from defective nuclear distribution rather than
145 defective blastoderm patterning, we focused our analyses on the distribution of cortical nuclei during
146 cellularization, i.e., just before gastrulation, using fixed embryos stained for DNA to visualize nuclei in the
147 embryo volume (see methods). In embryos developing at 29°C, we observed a subcortical cluster of nuclei in
148 a small fraction of embryos, corresponding to a hole in the cortical layer of nuclei (Figure 2A). To better
149 visualize and differentiate cortical and subcortical nuclei, we segmented the embryo volume and color-coded
150 the image voxels based on their distance from the embryo surface (Figure 2B). We noticed a few subcortical
151 nuclei in embryos developing at normal temperature (Figure 2C, F, I, J), while a large fraction of embryos
152 developing at 29°C showed an increase in subcortical nuclei, albeit not in large clusters (Figure 2D, G, K , L).
153 Notably, however, in a small fraction of embryos developing at 29°C, we observed a notable void in the
154 cortical layer of nuclei (henceforth, blastoderm hole), coinciding with a subcortical cluster of at least 10 nuclei
155 (Figure 2E, H, M, N). Within the coordinate system of the embryo, the distribution of neither isolated
156 subcortical nuclei nor blastoderm holes was left-right symmetric. Additionally, even if blastoderm holes were
157 predominantly observed in the central region of the embryo, their location varied in their position across
158 embryos (Figure 2O, P). These results further support the idea that loss of nuclei and blastoderm holes are
159 unlikely to be directly caused by defective patterning: embryonic patterning is left-right symmetrical and
160 accordingly, observed defects in patterning would likewise show left-right symmetry.

161 To investigate the underlying cause for the appearance of subcortical nuclei, we followed nuclear dynamics
162 using time-lapse recordings: Histone-RFP was used to visualize chromatin, and Jupiter-GFP to visualize
163 microtubules for keeping track of nuclear division cycles. Starting with the first appearance of nuclei at the
164 embryo cortex (occurring during the interphase of the 10th nuclear cycle), we observed nuclei through their
165 cortical divisions during syncytial blastoderm (through mitoses 10 to 13), then through cellularization
166 (interphase 14), and until the onset of gastrulation (beyond interphase 14). To determine whether the
167 nuclear loss at 29°C reflects a threshold response associated with a transition to non-Arrhenius behavior, we
168 examined temperature dependencies additionally at 22°C, 25°C, and 28°C, temperatures within the normal
169 physiological range.

170 The cortical arrival of nuclei during interphase 10, from the yolk to the embryo cortex, was comparable
171 between embryos developing at 22°C, 25°C, 28°C, and 29°C (Figure 3A-E, top panels), indicating that the
172 preblastoderm stage spreading of nuclei along the AP axis[22] was comparable between these temperatures.
173 During the syncytial blastoderm stage and cellularization, however, embryos that developed at 29°C much
174 more frequently "lost" nuclei from their cortical layer than those developing at 22, 25, and 28°C, i.e., nuclei
175 that were initially positioned within the cortical layer of the egg, appeared to get expelled, descended into
176 the yolk, and did not become part of the embryonic blastoderm (Figure 3, also see below), with variability in
177 the extent of the nuclear loss, producing blastoderm holes in a fraction of embryos (Figure S1).

178 Taken together, in pre-gastrulation embryonic development we narrowed down the developmental
179 vulnerability at 29°C to the syncytial blastoderm stage and cellularization, where we see nuclear loss from
180 the embryo cortex. Notably, the fraction of embryos showing blastoderm holes (Figure 2A, Figure S1) was
181 similar to the fraction of embryos with gastrulation defects (Figure 1F) and was consistent with embryo
182 lethality at 29°C (Figure 1B). The embryo-to-embryo variability, both in the distribution and intensity of
183 nuclear loss, further supports the argument that these defects were not dictated by defective embryonic
184 patterning, and were likely caused by defects in non-deterministic self-organised processes. While consistent
185 with the idea that the presence of blastoderm holes was causing the observed increase in embryonic lethality,
186 the temperature-dependent mechanism leading to blastoderm holes was still unclear. To further address the
187 mechanistic link between elevated temperature and embryo lethality, we decided to quantify the loss of
188 nuclei and possible patterns that could be predictive of blastoderm holes.

189 **At elevated temperature, embryos lose nuclei from the cortex after defective divisions.**

190 Closer analyses of lost cortical nuclei indicated that these nuclei were lost either individually or as pairs of
191 two adjacent nuclei. To identify their relative contribution to the early developmental vulnerability at
192 elevated temperatures, we decided to quantify these two types of nuclear loss from the embryo cortex.

193 Our analyses first focused on the isolated loss of nuclei. An isolated nucleus could be lost by a division
194 perpendicular to the embryo surface (out-of-plane division), where the nucleus facing the inside of the
195 embryo may not get properly anchored to the cortex and is consequently lost into the yolk. Alternatively, an
196 isolated nucleus may be lost after an in-plane division, e.g. if steric hindrance and insufficient space would
197 not allow for simultaneous anchoring of two adjacent nuclei to the embryo cortex. To account for these
198 possibilities, we visually tracked every individually lost nucleus back in time to its last division.

199 Out-of-plane divisions could be detected in embryos at all of our experimental temperatures. These out-of-
200 plane divisions could be easily identified, as they formed a characteristic mitotic spindle that was oriented
201 perpendicular to the embryo surface (Figure 4A), and after the division only one of the daughter nuclei
202 remained attached to the cortex. However, out-of-plane divisions occurred only during the mitoses of the
203 10th nuclear cycle, thus couldn't explain the loss of nuclei from the 11th nuclear cycle onwards. Loss of nuclei
204 following an in-plane division could also be detected. These losses occurred at a low frequency throughout
205 the syncytial blastoderm stage and cellularization, at all tested temperatures (Figure 4B). When we quantified
206 the isolated loss of nuclei, we noted that (i) the overall frequency of out-of-plane divisions was very low (<5%)
207 (Figure 4C), (ii) loss of individual nuclei after an in-plane division was rather infrequent, and, even if slightly
208 more frequent during interphase 14 (cellularization), (iii) the loss of individual nuclei did not differ
209 significantly within the range of experimental temperatures (Figure 4D). The overall extremely low frequency
210 of isolated nuclear loss – even in embryos developing at 29°C – strongly suggests that isolated nuclear loss
211 was not the main driver of temperature-dependent nuclear loss in the fly blastoderm.

212 Next, we focused on the pairwise losses of nuclei. As above, we tracked lost pairs of nuclei to their last division
213 cycle. This tracking revealed that every pairwise loss of nuclei was, in fact, a loss of sister nuclei. This
214 observation suggested that specific characteristics of cortical nuclear divisions might determine the future
215 fate of the newborn nuclei and trigger their release from the egg cortex, possibly in response to failed
216 checkpoints. Consistent with this idea, we observed chromosome segregation defects, and a delay in
217 telophase, preceding the pairwise loss of nuclei (Figure 4E), at all of our experimental temperatures. Because
218 chromosome segregation defects can lead to aneuploidy, our observations suggested that the subsequent
219 expulsion of daughter nuclei from the egg cortex was due to prior defective mitosis. To address whether the
220 observed loss of nuclei at 29°C could be attributed to an overall increase in defective mitoses, we asked if
221 their frequency was changing depending on the temperature (see methods). For this, we focused on
222 interphase 14, which is when we observed the most nuclear losses. While the frequency of mitotic failures
223 was overall low at 22 to 28°C, it increased significantly at 29°C (Figure 4F). Of note, defective mitoses, both
224 at normal or at elevated temperature, were not associated with a stereotypical time course of nuclear
225 expulsion. Defective nuclei could be lost in the interphase immediately following defective divisions, or later
226 (Figure S2), suggesting that nuclear expulsion after defective mitosis was a passive process and not triggered
227 by molecular signaling at failed checkpoints.

228 Taken together, our findings identify nuclear divisions in the blastoderm as a thermolabile cellular process
229 that shows a disproportionate increase in failures with the transition from 28°C to 29°C, resulting in the loss
230 of sister nuclei from the egg cortex, when born in defective mitoses. However, which characteristics of
231 nuclear divisions render them thermolabile was unclear.

232 **At elevated temperature, nuclei displace drastically, especially during divisions.**

233 For embryos at 25°C, we noted that the nuclei were rather dynamic in their localization, showing local
234 movements, throughout the syncytial blastoderm stage. For embryos at 29°C, this dynamicity increased, and
235 we could see nuclei being displaced rather drastically. We hypothesized that such displacement poses a
236 challenge to nuclear anchorage at elevated temperatures, especially during mitosis, causing mitotic defects
237 and the paired loss of nuclei. To that end, we tracked nuclear groups starting from individual mother nuclei
238 at end of interphase 10 to the 8 great-granddaughter nuclei at end of interphase 13. At each time point, we
239 computed the center of the nuclear group, using the positions of the nuclei in that group, yielding one track
240 per group (Figure 5A-C, also see methods). Our tracking showed that the centers of nuclear groups had two
241 components to their movement, a global drift and a local displacement.

242 First, the nuclear groups exhibited a global consistent drift-like movement, which represented a concerted
243 global movement of all nuclei. We captured this component using a linear fit to the tracks of the center of
244 the nuclear groups over time (Figure 5B dotted lines). The slope of the linear fit indicated that the groups
245 drifted towards the posterior end at all of our experimental temperatures (Figure 5D, E). This component of
246 nuclear movements was reminiscent of the previously reported dynamic reordering of nuclei in the early
247 syncytial blastoderm[23]. Notably, however, the extent of drift in nuclear groups did not correlate with the
248 occurrence of blastoderm holes (Figure 5D, hollow markers).

249 Second, independent of this drift, we observed local deviations in the position of the nuclear groups over
250 time. We decided to measure these local deviations relative to the global drift. We reasoned these local
251 deviations could be a proxy for mechanical stresses experienced by the nuclear division machinery, and
252 quantified these deviations during interphase-metaphase and anaphase-telophase. The deviations relative
253 to the constant drift were more drastic along the anterior-posterior (AP) axis (Figure 5F, H) than those along
254 the dorsal-ventral (DV) axis (Figure 5G, I), and deviations during the anaphase-telophase period (Figure 5H)
255 were more drastic than those during the interphase-metaphase period (Figure 5F). In the context of length

256 scales typical for nuclear divisions, this meant that nuclear group deviations in embryos developing at 25°C
257 and during anaphase-telophase were comparable to that of the length of the spindle itself, while for embryos
258 at 29°C, nuclear group deviations could be up to 4-fold higher. This increase in nuclear group deviations
259 suggested increased mechanical stresses especially during the critical anaphase-telophase period, indicating
260 an extensive propensity for displacement relative to embryo cortex at a time when the dividing nuclei need
261 to be robustly anchored to the embryo cortex. Consistent with this interpretation, embryos with blastoderm
262 holes showed the highest nuclear group deviations especially during anaphase-telophase (Figure 5H, large
263 hollow markers).

264 To further test the link between mitotic failures and the short-range local nuclear displacements, i.e., nuclear
265 group deviations, we followed the division of each of the 8 great-granddaughter nuclei in every tracked
266 nuclear group at 29°C from mitosis 13 to interphase 14, expecting to see mitotic failures in nuclear groups
267 with greater displacements. Here, however, we failed to see a correlation between extent of nuclear group
268 deviations and a subsequent mitotic failure (Figure 5J). In that, the nuclear groups with one or more
269 subsequent mitotic failures (Figure 5J, hollow markers) do not show particularly higher deviations compared
270 to their normally dividing counterparts. In fact, when we count the number of nuclear groups with
271 subsequent mitotic failure defects, we see that 15 of these groups were below their respective embryo
272 medians, while only 7 are above, arguing against a correlation between increased nuclear displacements and
273 subsequent mitotic failures during interphase 14.

274 In addition to the analysis of nuclear movements parallel to the embryo cortex we wondered about the
275 movements orthogonal to cortex, i.e., the future apical-basal (AB) axis in the blastoderm cells[24]. In embryos
276 developing at 25°C, we observed that nuclei maintained a constant distance from the cortex (Figure S3A).
277 However, in embryos developing at 29°C, we could see two waves of nuclear displacement towards the
278 cortex, which originate from the anterior and the posterior, and meet at the central region of the embryo
279 (Figure S3B). These waves of nuclear displacement were tightly correlated with waves of nuclear divisions,
280 with peaks of the waves corresponding to anaphase-telophase transition. This suggests that as nuclei divide
281 the spindle moves upwards, presumably to gain more space. This need for space indicated additional
282 challenges for the spindles during nuclear division, explaining, at least in parts, the mitotic failure at 29°C.

283 Taken together, our quantifications and observations captured an embryo-wide increase in nuclear
284 displacement locally, along the AP- and AB-axis. In a fraction of embryos, the mitotic failures occurred in
285 great numbers and in close vicinity, leading to holes in the blastoderm epithelium at 29°C (Figure 4F, hollow
286 markers), and these embryos also exhibited greater displacement of nuclei during anaphase-telophase
287 (Figure 5H, hollow markers). Notably, however, our quantifications and observations of an increased nuclear
288 displacement could not reveal any correlation with nuclear loss at the level of individual nuclear groups
289 (Figure 5J). This result argues against the idea of increased dynamicity being the cause of nuclear division
290 defects at 29°C. Thus, although the formation of blastoderm holes (Figure S1) could be directly attributed to
291 clustered mitotic failures, it remained unclear why mitotic failures were stochastically distributed in most
292 embryos, yet locally clustered in the central region of a small fraction of embryos, producing blastoderm
293 holes.

294 **Nuclei are crowded and divide with a time shift in embryos at elevated temperature.**

295 To better understand the differences between stochastic mitotic failures and locally clustered failures, we
296 focused on cases with severe nuclear losses in embryos at 29°C. The most severe loss of nuclei in embryos at
297 29°C was often observed during cellularization (interphase 14) in the central domain of the embryo (Figure
298 2, 3 and S1). Thus, we wondered if the central regions of the embryo were somehow special, and if there

were characteristics in nuclear distribution or nuclear division, already during nuclear cycle 13, that rendered the central regions to be distinct than the anterior/posterior poles.

The central region of the embryo had more tightly packed nuclei, indicating a defect in self-organized nuclear reordering mechanisms[23]. To quantify this nuclear crowding, we focused on the end of interphase 13 (see methods), as that's the time we observed maximum nuclear crowding, before the most intense nuclear loss. To quantify the space available for cortical blastoderm nuclei, we segmented the nuclei and used Voronoi tessellation to define a region around each nucleus, which we call pseudo-cells. The areas of pseudo-cells were rather homogeneous in embryos developing at 22°C (Figure 6A, E, I). Already at 25°C (Figure 6B, F, J) and 28°C (Figure 6C, G, K), the available space for cortical nuclei was no longer uniform across the embryo, and it showed signs of local crowding in the central regions of the embryo. At 29°C, the space available for nuclei along the anterior-posterior axis varied substantially and revealed strong nuclear crowding in the central region of the embryo (Figure 6D, H, L). We quantified the extent of crowding (see methods), and found a progressive increase in nuclear crowding (Figure 6M), with peak crowding at 29°C. To specifically test whether the central region of the embryo was distinct from the poles in inter-nuclear spacing, we quantitatively described elevated nuclear crowding at 29°C in the central region of the embryo (Figure 6N).

The central regions of the embryos at 29°C coincided with the "collision" of two waves of nuclear divisions starting from the poles (see above, Figure S3). This observations was in stark contrast with embryos at 25°C, where nuclear divisions are meta-synchronous[25], with anterior-posterior waves (Figure 6O). We could further observe that in contrast to the meta-synchrony at 25°C, phases of nuclear division in the central region at 29°C were lagging behind those at the anterior/posterior pole of the embryos (Figure 6P). Accordingly, the same phase of the nuclear division cycle could be observed at different time points in different regions of the embryo (Figure S4A-B), indicating defects in the self-organised coordination of nuclear division cycles across the syncytium[25]. Thus, we decided to quantify this asynchrony of nuclear division cycles at temperatures 22°C, 25°C, 28°C, and 29°C, as nuclei exited nuclear cycle 13 and entered cycle 14 (see methods). Our quantifications show that the asynchrony significantly increases in embryos developing at 29°C as compared to other temperatures (Figure 6Q). This indicated that the central region of the embryo is distinct from the poles in nuclear division dynamics, with the phases of the nuclear cycle lagging (Figure 6R).

Taken together, ~~i~~n the central region of the *Drosophila* syncytial blastoderm embryo, nuclear division cycles lag behind those at the anterior/posterior poles, and nuclear density is greater than that at the anterior/posterior poles. Given that blastoderm holes also appear in the central regions of the embryo, we tested whether the clustering of mitotic failures (leading to blastoderm holes) at 29°C correlated better with the regions of highest nuclear crowding, or the most delayed nuclear cycles, or both.

Region of embryo with greater nuclear crowding and with delayed nuclear cycles are associated with greater frequency of mitotic failures.

To test whether nuclear crowding and/or nuclear cycle asynchrony resulted in a predisposition towards a local increase in mitotic failure, we first defined the regions of the embryo with high nuclear crowding (Figure 7A) at the end of interphase 13, or regions with substantially delayed nuclear division cycles (Figure 7B) at the end of mitosis 13. In parallel, we marked the locations of mitotic failures occurring during cellularization (interphase 14), which could be overlaid on any predefined region to calculate the fraction of mitotic failures in that region. Then, to measure the fraction of mitotic failures associated with either nuclear crowding, or nuclear cycle asynchrony, or both, we constructed the regions of the embryo with either high nuclear crowding, i.e., crowded regions (Figure 7C); or substantial delay in nuclear division cycles, i.e., delayed regions (Figure 7D); or a combination of crowded and delayed regions, i.e., combined region (Figure 7E) (see methods).

343 In crowded regions, the fraction of mitotic failures increased progressively with higher temperatures, with
344 statistically significant differences between 22 and 29°C (Figure 7F). In delayed regions, the fraction of mitotic
345 failures showed an abrupt increase from 28 to 29°C, albeit with only marginal statistical significance (Figure
346 7G). In the combined regions, the fraction of mitotic failures was greater than those in the crowded or
347 delayed regions alone (Figure 7H). Additionally, the fraction of mitotic failures in all of the tested
348 temperatures could not be explained by the area fractions themselves (Figure 7I-K). This suggests that the
349 combination of nuclear crowding and nuclear cycle asynchrony contributes to a temperature-dependent
350 predisposition toward mitotic failure in the syncytial blastoderm, with nuclear crowding exerting the stronger
351 influence.

352 One plausible mechanism is that local nuclear crowding limits the space for proper mitotic spindle formation,
353 thereby increasing the likelihood of mitotic errors. In addition, crowding may locally elevate the Nuclear-to-
354 Cytoplasmic (N/C) ratio, a parameter that reflects the amount of cytoplasm available to each nucleus. The
355 N/C ratio is known to regulate the pace of nuclear division cycles, such that higher N/C ratios are associated
356 with slower nuclear division cycle[25–30], likely due to limited cytoplasmic resources required for the cell cycle.
357 Nuclear crowding would therefore slow nuclear cycle indirectly through its effect on N/C ratio. Consistent
358 with this interpretation, the reduced area of the 'combined regions' at 29°C (Figure 7K) indicates substantial
359 spatial overlap between crowded regions and delayed regions, particularly in embryos exhibiting blastoderm
360 holes. Thus, at elevated temperature, these combined regions likely reflect both the direct mechanical
361 consequences of crowding and its indirect effects mediated through altered nuclear division timing.

362 Taken together, the spatial overlap between nuclear crowding and nuclear cycle asynchrony helps explain
363 why clustered mitotic failures arise preferentially in the central region of the embryo, leading to blastoderm
364 holes. However, while this framework clarifies where and how mitotic failures are spatially organized, it does
365 not explain why elevated temperature enhances their frequency. This raises the question of how elevated
366 temperature perturbs mitosis at the molecular level.

367 **Mitotic failures trigger DNA damage response**

368 To distinguish whether the observed loss of nuclei were primarily caused by temperature-induced DNA
369 damage leading to mitotic failure, or instead by a temperature-induced failure of mitosis that subsequently
370 resulted in damaged DNA, we employed a previously described DNA damage reporter system[31]. Briefly, this
371 reporter relies on the nuclear localization of Stem-Loop Binding Protein (SLBP), which normally shuttles
372 between nucleus and cytoplasm during interphase, exporting the mRNAs for key early zygotic genes[31].
373 Following DNA damage, Chk2 phosphorylates SLPB at Serine 118, thus restricts nuclear localization of SLBP,
374 targeting the protein to degradation. Thus, exclusion of SLBP from the interphase nucleus can act as a live
375 marker for DNA damage in that nucleus (Figure 8A), provided that the nuclear envelope remains intact.

376 To determine the cause for the cortical loss of nuclei, we used the absence of SLBP nuclear accumulation as
377 an indicator for DNA damage and followed such nuclei over a nuclear division cycle. All nuclei displaying
378 evidence of DNA damage were mitotically arrested and were subsequently lost into the interior of the
379 embryo (Figure 8B). DNA damage therefore consistently coincided with mitotic failures and, just like the
380 mitotic failures, affected sister nuclei.

381 To quantify the kinetics of SLBP nuclear localization over the different phases of the nuclear division cycle,
382 we measured SLBP-GFP nuclear intensity from late interphase 13 through early interphase 14. SLBP showed
383 high nuclear localization at the end of interphase 13, was then excluded from the nuclei during mitosis, and
384 progressively re-accumulated in nuclei at the onset of interphase 14 (Figure 8C, F). This behavior was
385 comparable between 25 and 29°C during normal nuclear divisions. In contrast, following mitotic failure, we

386 observed a progressive reduction in SLBP nuclear localization within the first ~4 min of interphase 14,
387 followed by a more pronounced loss over the next ca. 10 minutes (Figure 8F), after which the nuclei were
388 typically expelled from the forming blastoderm. The absence of differences in SLBP localization during the
389 preceding interphase, together with indistinguishable behavior during mitosis, indicates that activation of
390 the DNA damage response occurs specifically during interphase 14 and only after the mitotic failure.

391 Mitotic failure can trigger a variety of signaling responses, raising the possibility that the observed loss of
392 SLBP nuclear localization reflects a response other than the DNA damage signaling. To address this, we
393 followed the nuclear localization of SLBP.S118A-GFP, a point mutant that cannot be phosphorylated at serine
394 118 and is therefore insensitive to Chk2-mediated DNA damage signaling[31]. Quantification of SLBP.S118A
395 nuclear localization revealed behavior comparable to wildtype SLBP in normally dividing nuclei (Figure 8D,
396 G). In nuclei with DNA damage, however, SLBP.S118A was retained in the nucleus during the early phase of
397 interphase 14, remaining detectable for approximately 4-5 minutes, before being progressively lost from the
398 nucleus at later time points (Figure 8G). These observations suggest that the loss of nuclear SLBP following
399 mitotic failure comprises at least two components; an early, DNA damage-dependent component and a later
400 component that is independent of SLBP phosphorylation at serine 118.

401 DNA damage can induce nuclear envelope destabilization, resulting in the release of nuclear proteins,
402 including SLBP. To contextualize the similarities and differences in the kinetics of SLBP and SLBP.S118A, we
403 therefore analyzed the behavior of a GFP reporter bearing a nuclear localization signal (NLS-GFP). In normally
404 dividing nuclei, NLS-GFP showed nuclear localization dynamics similar to those of both SLBP and SLBP.S118A
405 (Figure 8E, H). In contrast, following mitotic failure, the kinetics of NLS-GFP localization closely resembled
406 those of SLBP.S118A, but not wildtype SLBP (Figure 8F-H). This indicates that the altered nuclear localization
407 observed specifically during the early phase of interphase 14 reflects activation of the DNA damage response,
408 which is captured by SLBP-GFP but absent in both SLBP.S118A-GFP and NLS-GFP.

409 To quantify this DNA damage-dependent effect, we compared the rates of nuclear accumulation during the
410 initial phase of interphase 14. SLBP nuclear import was significantly slower in nuclei undergoing division
411 defects at 29°C compared to normally dividing nuclei at the same temperature (Figure 8I). In contrast, nuclear
412 import rates of both SLBP.S118A (Figure 8J) and NLS (Figure 8K) were unaffected by mitotic failure during this
413 early interphase period.

414 Taken together, these results indicate that DNA damage arises as a consequence of mitotic failure rather
415 than acting as its primary cause. Moreover, the DNA damage response is rapidly engaged, becoming
416 detectable within minutes after entry into interphase 14. This rapid onset highlights mitosis as a critical point
417 of vulnerability and underscores the importance of understanding the mechanisms underlying mitotic failure
418 in order to improve embryonic robustness at elevated temperatures.

419 **Cytoskeletal dynamics during mitosis at elevated temperature**

420 Our results so far link the vulnerability of mitosis at elevated temperature – and its central role in the
421 formation of blastoderm holes – with embryo lethality at elevated temperature. Given the essential roles of
422 the cytoskeletal elements, F-actin and microtubules, in orchestrating mitosis, we next asked whether
423 elevated temperature alters cytoskeletal dynamics during syncytial nuclear divisions. Specifically, we
424 quantified changes in cytoskeletal organization during mitosis at 29°C as compared to 25°C, and examined
425 how these dynamics differed between normally completing divisions and mitotic failures.

426 During syncytial divisions, cortical F-actin undergoes extensive remodeling across the nuclear division cycle,
427 most prominently supporting the formation of the transient pseudo-cleavage furrows during mitosis[15,24,32].
428 These furrows progressively deepen perpendicular to the embryo surface while elongating parallel to it,

429 encapsulating the microtubule spindle throughout division. The spindle axis aligns with the long axis of the
430 pseudo-cleavage furrow (Figure 9A), and proper spindle elongation is essential for faithful chromosome
431 segregation. Defects in pseudo-cleavage furrow formation and/or mitotic spindle organization are therefore
432 expected to compromise mitotic fidelity.

433 Based on these considerations, we visualized F-actin-based pseudo-cleavage furrows and microtubule-based
434 mitotic spindles simultaneously in the same embryos, and quantitatively compared their morphology
435 between 25°C and 29°C, as well as between normal divisions and mitotic failures.

436 During mitosis, F-actin caps are elongated and expand to fill the cortical space, thereby outlining the pseudo-
437 cleavage furrows. Using these outlines, we measured the area of the F-actin caps and estimated aspect ratio
438 by fitting an ellipse, which also allowed us to determine the orientation of the long axis (Figure 9A). In parallel,
439 to characterize microtubule spindle geometry, we measured spindle length by connecting the spindle poles
440 and extracted the orientation of the spindle axis (Figure 9A). Qualitatively, both F-actin caps and microtubule
441 spindles appeared intact and comparable in overall intensity and structure across conditions, with the
442 notable exception of their relative alignment (Figure 9B-E). This prompted a quantitative comparison of F-
443 actin cap and spindle geometry.

444 We found that F-actin caps were significantly larger at 29°C than at 25°C, both in normally completing
445 divisions and in divisions that subsequently failed (Figure 9F), while their aspect ratios remained comparable
446 across conditions (Figure 9G). In contrast, spindle length was selectively reduced in divisions that went on to
447 fail, irrespective of temperature (Figure 9H). Consistent with this observation, spindles associated with
448 mitotic failures at 29°C showed little to no net elongation during mitosis (Figure 9I).

449 Together with the increased F-actin cap area, the reduction in spindle length indicated that the distance
450 between spindle poles and the cortical F-actin network is increased at elevated temperature, especially in
451 case of mitotic failures. Under these conditions, spindles appeared less constrained by the cortex and were
452 frequently observed to rotate. To quantify this behavior, we measured changes in spindle orientation
453 between consecutive time points throughout metaphase and summed these angular displacements.
454 Cumulative spindle rotation was significantly higher at 29°C than at 25°C, both in control divisions and in
455 mitotic failures (Figure 9J). In addition, spindle axes were often misaligned with the long axis of the
456 corresponding F-actin caps. Quantification of the angular mismatch between spindle and cap orientations at
457 metaphase confirmed that this misalignment was increased at 29°C in both control divisions and mitotic
458 failures (Figure 9K).

459 Taken together, these analyses indicate that mitotic spindles are less securely anchored to cortical F-actin at
460 elevated temperature. We propose that this weakened coupling increases the susceptibility of spindles to
461 rotational instability, thereby elevating the probability of mitotic failure. In combination with the spatial bias
462 of mitotic failures toward central regions of the embryo and the tight coupling between mitotic failure and
463 subsequent DNA damage, these findings identify mitotic failure as the primary driver of developmental
464 vulnerability at elevated temperature.

465 **Testing robustness of cell polarity establishment during syncytial divisions at elevated temperature**

466 Our findings thus far identify mitosis in the early blastoderm as a temperature-labile process and link mitotic
467 failure to embryo lethality at elevated temperature. This raised the question of how a deeply conserved and
468 generally robust process such as mitosis could become destabilized over a narrow temperature range. We
469 therefore asked whether increasing the abundance of key components of the nuclear division machinery
470 could compensate for temperature-induced fragility and restore developmental robustness at 29°C.

471 A distinctive feature of syncytial divisions in the *Drosophila* blastoderm is their reliance on transient pseudo-
472 cleavage furrows, which are repeatedly assembled and disassembled at each nuclear cycle. These furrows
473 form through localized membrane insertion from late interphase to metaphase, support the alignment of
474 mitotic spindles parallel to the embryo surface during pro- and metaphase, and regress rapidly during
475 anaphase and telophase. As a consequence, each nuclear cycle requires the repeated reestablishment of
476 cortical polarity cues alongside extensive cytoskeletal reorganization[24]. This dependence on transient cortical
477 polarity represents a major deviation from canonical cell division in fully cellularized tissues and may
478 constitute an evolutionarily young and potentially labile feature of insect embryogenesis. Moreover, polarity
479 signaling is closely intertwined with orientation of mitotic spindles[33], and cytoskeletal organization in
480 epithelia[34]. We therefore tested whether temperature sensitivity during syncytial mitoses reflects insufficient
481 robustness of polarity establishment: we aimed to strengthen polarity signaling through overexpression of
482 two key polarity regulators active in the early blastoderm, Bazooka (baz; Par-3 homolog) and Discs-large
483 (dlg)[35]. Specifically, we asked whether either overexpressions could rescue embryo lethality at 29°C, and if
484 so, whether this rescue was accompanied by a reduction in mitotic failures in crowded and combined regions
485 of the blastoderm.

486 In embryos at 25°C, we did not observe a significant change in embryo lethality with either *baz* or *dlg*
487 overexpression as compared to control embryos with wildtype levels of baz and dlg (Figure S5A). At 29°C,
488 lethality increased in control embryos (Figure S5A), similar to results in previous experiments (Figure 1B). By
489 contrast, embryos with either *baz* or *dlg* overexpression performed notably better at 29°C, with lethality
490 reducing to about two-thirds (*baz* overexpression) and half (*dlg* overexpression) of the controls (Figure S5A).
491 We note however that the rescue of lethality at 29°C in *baz* overexpressing embryos was only marginally
492 significant, with a lot of variability between samples. Additionally, *dlg* overexpressing embryos at 25°C
493 showed higher variability in embryo lethality than their control counterparts. Consistent with these results,
494 *baz* overexpression did not rescue the increase in the fraction of mitotic failures, either in the crowded
495 regions or in the combined regions at 29°C (Figure S5B, C), and while the large blastoderm holes were absent
496 in these embryos, *baz* overexpression occasionally produced small gaps in blastoderm (Figure S5B, C). Then,
497 *dlg* overexpression rescued the increase in the fraction of mitotic failures only in the crowded region at 29°C
498 (Figure S5B, C), and while the large blastoderm holes were absent in these embryos, *dlg* overexpression
499 increased the fraction of mitotic failures at normal temperature in both, the crowded region and in the
500 combined region, occasionally producing small gaps in blastoderm (Figure S5B, C).

501 Taken together, these results indicated that polarity establishment during syncytial divisions is comparatively
502 robust to elevated temperature and that deviation from canonical polarity mechanisms are not, by
503 themselves, sufficient to explain temperature-induced mitotic failure. Instead, the partial rescue effects
504 suggest that the primary temperature-sensitive vulnerability lies downstream of polarity establishment, at
505 the level of cytoskeletal regulation required to anchor and stabilize the mitotic spindle. This led us to focus
506 on molecular interactions that directly link cortical F-actin to astral microtubules of the spindle during mitosis.

507 **Identifying vulnerabilities in cytoskeletal interactions during mitosis at elevated temperature**

508 Since strengthening polarity establishment was not sufficient to robustly suppress mitotic failures at elevated
509 temperature, we next turned to molecular interactions acting downstream of polarity cues that directly
510 execute spindle positioning and chromosome segregation. Proper assembly and anchoring of the mitotic
511 spindle at the cortex requires a dynamic interaction between microtubules and F-actin, which together
512 anchor chromatin at the cortex throughout nuclear division[24]. Faithful segregation of sister chromatids
513 therefore depends on tightly regulated interactions between the actin cortex and the astral microtubules of
514 the mitotic spindle[36,37].

515 In *Drosophila*, these critical actin-microtubule interactions have been associated with a tripartite protein
516 complex consisting of α-Catenin (αCat), which associates with cortical F-actin; β-Catenin (βCat, or *armadillo*
517 in *Drosophila*), which binds to α-Catenin; and Adenomatous polyposis coli 2 (Apc2), which links to βCat and
518 binds to the astral microtubules of the mitotic spindle[38]. Within this complex, the interaction of αCat and
519 βCat is direct and appears constitutive, whereas the interaction of βCat and Apc2 is mediated by a specific
520 kinase, the *Drosophila* homolog of the Glycogen Synthase Kinase 3β, Shaggy (sgg)[39].

521 We reasoned that, if this tripartite protein complex was thermolabile, then our high temperature conditions
522 should, at least in parts, phenocopy the loss of function of one of the components of the complex (αCat,
523 βCat, or Apc2) or sgg. The loss of function of this protein complex has been associated with an "empty actin
524 caps" phenotype, where cortical dome-like structures of F-actin are no longer associated with nuclei[38]. Thus,
525 to test for the possibility that this tripartite protein complex is thermolabile during early embryonic
526 development in *Drosophila*, we analyzed embryos that were fixed and stained to visualize nuclei and cortical
527 F-actin (see methods), both at 25°C (Figure S6A) and 29°C (Figure S6B). At control temperature of 25°C, we
528 could observe a tight association between nuclei and F-actin during interphases in the syncytial blastoderm,
529 where cortical F-actin surrounds each nucleus, forming the actin cap. Notably, it was possible to identify gaps
530 between neighboring actin-caps in cases of recently expelled nuclei (Figure S6C), or in cases where the
531 spacing between nuclei is large enough (Figure S6D). Similar to embryos at 25°C, such gaps could also be
532 observed between neighboring actin-caps in cases of recently expelled nuclei at 29°C (Figure S6E). In contrast
533 to controls at 25°C, however, embryos developing at 29°C additionally exhibited the empty actin caps
534 phenotype (Figure S6F), reminiscent of embryos mutant for *Apc2* or β*Cat* (see Figure 3d-f in McCartney et al.
535 2001[38]). Thus, we hypothesized that stabilizing the activity of the complex, through elevated levels of αCat,
536 βCat, Apc2, or sgg, could increase the fidelity of cortical mitoses at 29°C, possibly through a tighter control of
537 actin and microtubule coupling. Such tighter coupling, in return, might decrease the fraction of mitotic
538 failures in crowded and combined regions and ultimately attenuate embryonic lethality.

539 To test the effects of elevated levels of either αCat or sgg on embryo lethality at control and elevated
540 temperatures, we overexpressed either gene and quantified embryo lethality. At 25°C, we did not observe a
541 significant difference in embryo lethality between control embryos and those with *αCat* or *sgg*
542 overexpression (Figure 10A). At 29°C, lethality was overall increased in controls, similar to results in similar
543 experiments described above (Figure 1B, Figure S5A). By contrast, embryos with either *αCat* or *sgg*
544 overexpression survived significantly better at 29°C, with lethality reducing to about half (*αCat*
545 overexpression) or a third (*sgg* overexpression) relative to the controls (Figure 10A). Consistent with these
546 results, large blastoderm holes were absent in these embryos, and the fraction of mitotic failures in crowded
547 as well as in the combined regions was reduced compared to control embryos at 29°C (Figure 10B, C). These
548 results suggest that overexpression either αCat or sgg strengthen the interaction between microtubule and
549 F-actin, which in turn attenuates temperature-dependent destabilizations of the mitotic spindle. We
550 therefore propose that the scaffolding activity of αCat, βCat, and Apc2, mediated by sgg, constitutes a
551 thermosensitive controller of nuclear division fidelity in the syncytial *Drosophila* embryo.

552 To test whether thermosensitivity of nuclear division fidelity was dependent specifically on the scaffolding
553 activity of αCat, βCat, and Apc2 rather than a common capacity of any regulator of mitotic spindle anchorage,
554 we asked whether the elevated levels of other regulators could similarly increase robustness against elevated
555 temperatures. To address this question, we focused on regulators known to dictate the orientation of the
556 mitotic spindle during cell division[40]. Both, the activity of 'Mushroom body defect' (mud, NuMA homolog)
557 and that of Inscuteable (insc) has been previously described to regulate the anchorage and orientation of the
558 mitotic spindle during cell division. A similar activity might be present for nuclear divisions during the
559 syncytial blastoderm stage, raising the possibility that an overexpression of *mud* or *insc* could rescue embryo

560 lethality, presumably by reducing mitotic failures. However, neither *mud* nor *insc* overexpression ameliorated
561 the high embryo lethality at 29°C (Figure S7), supporting the notion that elevated temperature specifically
562 challenges the core machinery of the mitotic spindle rather than being a non-specific failure that could be
563 rescued by any mitosis associated regulator.

564 **Thermosensitive regulators of spindle dynamics exhibit natural variation along thermoclines.**

565 While temperatures above 25°C are generally considered non-standard rearing conditions for *Drosophila* lab
566 strains, naturally occurring populations likely do experience temperatures above this presumed optimum
567 temperature. Since our analyses showed that elevated temperatures during the first hours of fly
568 development affect both, embryonic cell biology and organismal fitness, it may be tempting to predict that
569 natural populations could be adapting to temperature changes through standing genetic variation and
570 shifting allele frequencies in the same or similar genes that we identified as thermolabile regulators of nuclear
571 divisions. To address this possibility, we analyzed the distribution of standing genetic variations associated
572 with the regulators of spindle dynamics (Figure 10D) and asked whether genetic variation would be
573 distributed randomly with respect to the continent-scale gradients of annual mean temperature, i.e.
574 thermoclines. While most standing genetic variation associated with putative 'spindle dynamics' regulators
575 was indeed distributed without a clear thermoclinal pattern and did not allow for rejection of our null
576 hypothesis, (Figure 10E, Table S1, S2), *sgg* was a clear and notable outlier in this analysis and exhibited a
577 thermoclinal distribution of natural variations independently in populations in the North America, Europe,
578 and Australia. Additionally, the fraction of genes associated with 'spindle dynamics' that showed thermoclinal
579 pattern, was greater than the fraction of genes associated with the GO-term 'metabolic process' that showed
580 thermoclinal pattern (Figure 10E, Table S1, S2). These findings strongly suggest that the thermosensitivity
581 that *sgg* exhibits in lab conditions constitutes a biological property, which can be exposed and selected for
582 also in natural populations and during the course of evolution.

583 **Discussion:**

584 **Early fly development is susceptible to elevated temperature**

585 Our work demonstrates that processes of syncytial blastoderm formation and cellularization in *Drosophila*
586 embryonic development are vulnerable to elevated temperature. Embryos exposed to 29°C during these
587 stages exhibit defects in maintaining the bilateral symmetry of developmental processes, and in extreme
588 cases, enter a lethal trajectory during gastrulation (Figure 1). We argue that these extreme cases of
589 developmental failure likely coincide with structural defects in the blastoderm epithelium, which manifest as
590 regions devoid of nuclei/cells and discontinuities in this tissue (Figure 2, 3 and S1). The result is holes in the
591 blastoderm, which arise from a greater incidence of mitotic failures in a small region of the embryo during
592 syncytial nuclear divisions (Figure 4). Our analysis also establishes a link between mitotic failures and the
593 subsequent loss of nuclei, via DNA damage response (Figure 8). We show that mitotic failures trigger DNA
594 damage response in the defective daughter nuclei, which are then mitotically arrested, lose the integrity of
595 their nuclear envelop, and are "kicked-out" of the blastoderm. We note that the DNA damage repones is
596 active only in nuclei with DNA damage, and not in its normal neighbors. It remains to be determined whether
597 these lost nuclei deplete transcription factors required for local cell fate specification. This will, in turn, reveal
598 whether blastoderm holes cause gastrulation defects purely through mechanical discontinuity, or whether
599 loss of patterning information also contributes.

600 Our analysis shows that clustering of mitotic failures occurs in embryonic regions that lag behind in the
601 nuclear division cycle and exhibit nuclear crowding (Figure 6). While we treat these factors as independent
602 for most of their analysis, a combination of these factors – captured in 'combined regions' – predispose

603 particular regions of the embryo to increased mitotic failures at 29°C (Figure 7). Thus, our findings are
604 consistent with previous studies, which suggest that they are mechanistically coupled through the N/C
605 ratio[25–30]. These findings suggest a mechanism in which the dependence of nuclear cycle duration on nuclear
606 density could amplify the likelihood for mitotic failure at elevated temperature; whether a similar interplay
607 affects embryonic development under normal temperature conditions remains unclear.

608 Alternatively – or additionally – the source of vulnerability of early blastoderm formation could stem from
609 the non-deterministic distribution of nuclei, which relies on self-organization and is driven by the activity of
610 cytoskeletal elements such as F-actin and microtubules[23]. A related form of self-organization may be seen in
611 the progression of nuclear division cycles, which move across the surface of the embryo as non-deterministic
612 waves[25]. Both processes appear to be challenged at elevated temperatures, suggesting that developmental
613 mechanisms relying on biological self-organization may be particularly vulnerable at elevated temperature.
614 Given the widespread importance of self-organization in biology, it may be valuable to explore more
615 generally whether developmental processes that depend heavily on self-organizing components constitute
616 common points of vulnerability.

617 **Potential impact of elevated temperature on essential protein-protein interactions**

618 We show that mitosis itself is vulnerable at elevated temperatures due to weakened interactions between
619 microtubules and F-actin (Figure 9). The tripartite complex, involving αCat, βCat, and Apc2 (mediated by the
620 protein kinase sgg) has been implicated in mediating this interaction[38], at least partially, and in our
621 experiments overexpressing *αCat* or *sgg* rescue the developmental defects and embryo lethality at elevated
622 temperature (Figure 10A-C). These results support the idea that compromised coupling between
623 microtubules and F-actin represents a key molecular vulnerability at elevated temperature.

624 A mild temperature increase such as the one we studied here is unlikely to denature proteins, but may
625 instead weaken protein-protein interactions, such as the ones between components of the tripartite scaffold,
626 involving αCat, βCat, and Apc2 (mediated by the protein kinase sgg). Such weakening would effectively
627 deplete functional protein scaffolds, creating a loss-of-function-like scenario, as the equilibrium shifts
628 towards the dissociated state of the scaffold. Nuclear crowding can exacerbate this effect: in crowded
629 regions, individual nuclei experience a relative reduction in the local concentration of the scaffold owing to
630 an increase in the N/C ratio. Thus, the combination of elevated temperature and local crowding provides a
631 plausible mechanism for regional predisposition to mitotic failure and the formation of blastoderm holes.
632 This interpretation is consistent with the observation that overexpression of either *αCat* or *sgg* rescues these
633 defects (Figure 10A-C), as increasing even a single component should be sufficient to raise overall scaffold
634 abundance and counteract both temperature-dependent dissociation and crowding effects.

635 Independent support for this mechanistic framework comes from previous work in a different context. The
636 nuclear crowding defect we report here is reminiscent of a previous study, focusing on embryos with
637 increased maternal cyclin B, though at normal tempeatures[41]. While the impact of elevated temperature on
638 cyclin B activity remains to be characterized, this study found that genetic perturbations enhancing
639 microtubule-F-actin interactions suppress the phenotype. Even though the upstream perturbation differs
640 from heat stress, the convergence on the same interaction interface supports the view that microtubule-F-
641 actin coupling represents a common point of vulnerability.

642 Given that protein-protein interactions are omnipresent in biology, it is unlikely that microtubule-F-actin
643 coupling is the only process directly modulated by temperature, and other aspects of basic cell biology may
644 similarly be vulnerable. Because of their reliance on formation of protein scaffolds, it may be particularly
645 rewarding to assess potential temperature sensitivity in processes such as cellular signaling[42,43],

646 mitochondrial metabolism[44,45], cell polarity pathways[46,47], or the regulation of membrane trafficking[48], the
647 cell cycle[49], and cytoskeletal dynamics[50,51], all of which are conserved across animal kingdom.

648 **Elevated temperature is distinct from heat shock effects**

649 Previous studies in *Drosophila* have shown that temperatures of 33°C or higher trigger a classic heat-shock
650 response, characterized by *de novo* transcription heat-shock protein genes[52]. This response has been
651 observed across embryos[53], larvae, pupae[54,55], and adult flies[56], and overexpression of heat-shock proteins
652 such as hsp23 can increase embryo survival under acute heat stress[57]. Heat shock proteins, accordingly, are
653 often considered to act as capacitors, buffering cells against environmental and genetic variation[58,59].

654 However, the extreme temperatures that provoke a heat-shock response are only transiently encountered
655 in natural environments[55]. Consequently, these conditions may not impose strong selective pressure to
656 improve tolerance to sustained temperature increases associated with global warming. Supporting this, our
657 analyses of three continental datasets did not reveal consistent allelic variation in canonical heat-shock
658 genes. We can't exclude, however, that the lack of allelic variation stems from a limited standing genetic
659 variation, given their critical role in survival, precluding the evolution of thermoclinal distributions. In either
660 case, it is unlikely that heat-shock proteins would constitute a mechanism to improve developmental
661 vulnerability in face of global warming.

662 In contrast, we observed allelic variation in *sgg* along thermoclines, suggesting it has been shaped by natural
663 selection. Seasonal shifts in sgg allele frequencies provide additional evidence, whereas heat-shock genes
664 show no such pattern[60]. These observations suggest that while heat-shock proteins protect against acute
665 temperature fluctuations, they may not confer selective advantage under elevated average temperatures.
666 Instead, regulators of cytoskeletal interactions, such as sgg, could be targets of natural selection and serve
667 as mechanisms to mitigate the effects of gradual temperature increases.

668 **Early embryonic vulnerability to elevated temperatures: implications for insect survival and evolution**

669 Early developmental processes from fertilization to blastoderm formation are highly conserved across
670 insects[61,62], suggesting that the vulnerabilities we report in *Drosophila* embryos could apply to many other
671 species. Weakening of cytoskeletal interactions under elevated temperature leads to asymmetric nuclear
672 distributions, disrupting positional information for subsequent morphogenesis and increasing the risk of
673 embryo lethality. Such cellular vulnerabilities provide a mechanistic link between temperature stress and
674 developmental failure, one that may be broadly conserved across diverse insect taxa.

675 Flies and other insects are essential for ecosystem stability[63], and rising temperatures pose a tangible threat
676 to their survival. Reports of contemporary insect biodiversity loss[64,65] resonate with patterns of extinction
677 and diversification during past climatic fluctuations[66,67]. Although multiple abiotic factors contribute to these
678 historical trends[68–70], the current rapid rise in global temperature highlights heat stress as a unique relevant
679 driver. Limited data make it difficult to test whether past warming events directly drove innovation in
680 blastoderm architecture, but it is intriguing to speculate that early developmental processes may serve as
681 both vulnerabilities and substrates for evolutionary change.

682 By identifying the cellular and molecular "breaking points" of heat sensitivity during early development, we
683 can better predict which species and life stages are most at risk, guide conservation strategies, and even
684 explore genetic pathways that enhance developmental robustness. Understanding these mechanisms offers
685 a potential bridge from cell-biology to ecosystem-level predictions in a warming world.

686 **Materials and methods:**

687 Fly lines and genetics:

688 *OregonR* line was used as WT *Drosophila*, and *w1118* line was used for outcrosses.

689 *Histone-RFP* expresses RFP tagged version of His2Av. Insertion on 3rd chromosome. Bloomington Drosophila
690 Stock Center (BDSC) #23650.

691 *Jupiter-GFP* expresses GFP tagged version of the microtubule-binding protein Jupiter. Insertion on 3rd
692 chromosome. Always used in combination with *Histone-RFP*. Gift from Jan Felix Evers.

693 *NLS-GFP* expresses GFP tagged Nuclear Localization Signal peptide. Insertions of 2nd and 3rd chromosome.
694 Always visualized alongside Histone-RFP. BDSC #1691.

695 *UtrABD-GFP* expresses GFP tagged version of Actin-Binding Domain of Utrophin. Insertion on 3rd
696 chromosome. Always used in combination with *Histone-RFP* and *Jupiter-GFP*. Gift from Thomas Lecuit.

697 *67-Gal4* (mat αTub-GAL4-VP16) is a maternal specific Gal4 driver. Insertion on 2nd chromosome. Always used
698 in combination either with *Histone-RFP* or *Histone-RFP* and *Jupiter-GFP* in the overexpression experiments
699 (see below). Gift from Thomas Lecuit.

700 *SLBP-* and *SLBP.S118A-GFP* expresses GFP tagged versions of SLBP and SLPB.S118A under UAS promoter.
701 Insertions on 3rd chromosome. Gifts from Eric Lecuyer. For these overexpression experiments, we first
702 crossed virgins from the Gal4 line '+; 67-Gal4; Histone-RFP' to the males of overexpression line '+; +; UAS-X'
703 (X= *SLBP*, or *SLBP.S118A*). F1 virgin females from these crosses were backcrossed to males of the paternal
704 genotype.

705 The following lines were used to drive the overexpression of various genes of interest in an attempt to rescue
706 the effects of 29°C. *baz*, BDSC #17613; *dlg*, BDSC #15779; *αCat*, BDSC #65590; *sgg*, BDSC #15886; *mud*, BDSC
707 #22371; *insc*, BDSC #39676. An outcross to *w1118* was used as control. For these overexpression
708 experiments, we first crossed virgins from the Gal4 line '+; 67-Gal4; Jupiter-GFP, Histone-RFP' to the males
709 of overexpression line 'UAS-Y; +; +' (Y= *baz*, *dlg*, *sgg*, or *mud*) or '+; +; UAS-Z' (Z= *αCat*, or *insc*), or to males of
710 *w1118* as control. F1 virgin females from these crosses were backcrossed to males of the paternal genotype.

711 Genotypes associated with various figure panels are listed in Table S3.

712 Embryo collection: For any experiment, males and females of appropriate genotypes (Table S3) were placed
713 into transparent cylindrical embryo collection cages (inner diameter ~5 cm). The cage top was closed with
714 fine-wire mesh for air exchange, and bottom with apple-juice agar plates. We prepared the apple-juice agar
715 plates from 1 l of solution: we boiled 24 gm of agar in 750 ml of water, adding 250 ml of fresh store-bought
716 apple juice while stirring on a hot plate, adjusting Sucrose to final amount of 25 gm (accounting for the sugar
717 content of the apple juice). This solution yielded ~80 petri dishes (6 cm diameter). After the agar solidified,
718 the plates were stored at 4°C. Before the embryo collection, the plates were covered with a thin layer of
719 yeast paste (to stimulate oviposition) and were pre-incubated to the embryo collection temperature for ≥30
720 min. Since *Drosophila* females can retain embryos long after fertilization, allowing early embryo development
721 inside their abdomen, we performed a 1 h "sham" embryo collection at room temperature (24-25°C), and
722 discarded these embryos. Following sham collections, we collected the embryos for experiments at specific
723 experimental temperature.

724 Embryo lethality experiment: We chose embryo-to-larva transition as a conservative and technically simple
725 read-out for embryo survival. This excludes any potential later-arising defects in viability, behavior, lifespan
726 or fertility, meaning that our assay underestimates, rather than overestimates, the deleterious effects of

727 elevated temperature. For estimating the survival, embryos were exposed to three temperature regimes
728 (Figure 1A). Depending on the regimen, we collected embryos for 1 hour either at 24-25°C (normal
729 temperature) or 29-30°C (elevated temperature). The 24-25°C collections were done on the bench top. The
730 29-30°C collections were done in a water bath, with embryo collection plate bottom in thermal contact with
731 the heated water. For NN or EN, we collected embryos for 1 hour at 24-25°C or 29-30°C, respectively, and
732 then incubated for 2 hours at the same temperature. The embryos were then bleached for 10-15 seconds,
733 rinsed thoroughly with tap water, aligned on a 24x60 mm coverslip, and covered with halocarbon oil. For NE,
734 we collected embryos for 1 hour at 24-25°C, incubated for 1.5 hours at the same temperature, and within 30
735 min processed as above (bleached, rinsed, aligned, and covered), and subsequently incubated for 3 hours at
736 29-30°C. After these treatments, embryos from all regimes were incubated at 24-25°C for ~1 day, following
737 which we counted the number of eclosed larvae and dead embryos. The embryonic lethality was calculated
738 as,

739 $$embryo\ lethality\ = \frac{100 * number\ of\ dead\ embryos}{number\ of\ dead\ embryos\ +\ number\ of\ larvae}$$

740 excluding the unfertilized embryos from calculations.

741 Imaging live embryos (after temperature treatment): Here we used 2 of the experimental temperature
742 regimes used in the 'Embryo lethality experiment' above, namely NN and EN. In short, we collected embryos
743 at 24-25°C (NN) or 29-30°C (EN) for 1 hour and then incubated the plate at the same temperature for another
744 2 hours. Then, the embryos were bleached for 35-40 sec, rinsed thoroughly with tap water, aligned with the
745 dorsal side facing a 22x40 mm coverslip, covered with halocarbon oil, and immediately taken for microscopy.
746 The embryos were recorded for at least 15 hours, at 25°C. Images were acquired on Leica SP8 DMi8 inverted
747 confocal microscope using 20x glycerol objective (0.75NA), at 2 µm step-size in z, and a final x-y resolution of
748 0.568 µm/pixel. We recorded the time-lapse at 1 frame every 4 min and recorded up to 5 embryos in parallel.

749 Imaging live embryos (at various temperatures): We used four temperature regimes. We collected embryos
750 for 1 hour either at normal temperatures (22-23°C, 24-25°C, or 27-28°C) or elevated temperature (29-30°C).
751 Collections at 22-23°C (22°C imaging) were done in the fly incubator; 24-25°C (25°C imaging) on the bench;
752 27-28°C (28°C imaging) or 29-30°C (29°C imaging) in a water bath, with embryo collection plate bottom in
753 thermal contact with the heated water. Then, the embryos are bleached for 35-40 seconds, rinsed with tap
754 water at the collection temperature, aligned on a 25 mm diameter coverslip, covered with halocarbon oil,
755 and immediately transferred to the temperature controller setup from Warner Instruments (QR-40LP holder
756 on QE-1HC heater/cooler, coupled to LCS-1 liquid cooling and CL-100 bipolar temperature controller,
757 precision of ± 0.1°C), pre-equilibrated to the experimental temperatures (22, 25, 28 or 29°C). For the data in
758 Figures 3-7, 10, S1-5, imaging was performed on Leica SP5 DMI6000CS inverted confocal microscope using
759 40x/1.1 NA water objective, 1x digital zoom, 2 µm z-steps (20 planes), and 0.379 µm/pixel x-y resolution;
760 acquiring images at 1 frame every 30 sec, 1 min, or 2 min depending on whether 1, 2, or 3-4 embryos were
761 recorded in parallel. For the data in Figures 8 and 9, the imaging was performed on Zeiss LSM 700 inverted
762 confocal microscope using 63x/1.2 NA water objective, 0.5x digital zoom, 2 µm z-steps (12 planes), and 0.198
763 µm/pixel x-y resolution; acquiring images at 1 frame every 30 sec or 1 min depending on the signal strength
764 for the genotype.

765 Imaging fixed embryos: We collected embryos for 3-4 hours either at 24-25°C (normal temperature) or 29-
766 30°C (elevated temperature). Collections at 24-25°C were done on the bench top; 29-30°C done in a water
767 bath, with embryo collection agar plate bottom in thermal contact with the heated water. Then, the embryos
768 were bleached for 40-45 seconds, rinsed with tap water, and fixed immediately. We only image and analyze
769 the embryos that are before the gastrulation stage. We performed two types of experiments; one, whole-

770 embryo nuclear imaging (Figure 2); and two, half-embryo imaging of nuclei and F-actin (Figure S6), using
771 distinct fixation/staining protocols.

772 For **whole-embryo nuclear imaging**, we used heat fixation and stained the embryos with DRAQ5. Briefly, we
773 transferred the processed embryos to 50 ml tubes, drained the excess water, added the boiled-to-turbidity
774 heat-fix solution (28% 500 µl NaCl + 5% 200 µl TritonX100 + 19.3 ml water), incubated for ~20 sec with
775 thorough mixing, and then immediately added water to cool down the mixture. Then, we transferred the
776 fixed embryos to 2 ml microfuge tubes, sequentially added n-heptane and methanol in equal proportions,
777 vigorously shook for ~30 sec to remove the vitelline membrane, and washed 3x with methanol. We started
778 the staining immediately after (though long-term methanol storage is possible). The embryos were
779 rehydrated with PBT (0.01% solution of Tween20 in PBS, 3 washes), stained with 1:1000 DRAQ5 for 1-hour,
780 washed 6x with PBT, re-suspended in 3:1 glycerol:PBS solution, and mounted between 2 rectangular
781 coverslips, with spacing optimized to immobilize the embryos w/o deforming them. Then we imaged the
782 embryos through both coverslips and the two halves stitched in image analysis (see below). Images acquired
783 on Leica SP8 DMi8 inverted confocal microscope using 20x/0.75 NA glycerol objective, 1.15x digital zoom, 1
784 µm z-step, and 0.247 µm/pixel x-y resolution.

785 For **half-embryo imaging of nuclei and F-actin**, we used formaldehyde fixation and stained the embryos with
786 DAPI and Phallacidin. Briefly, we transferred the processed embryos to a 20 ml vial containing the fixation
787 mix (3500 µl PBS + 37% 1000 µl formaldehyde + 4500 µl n-Heptane). The vial was shaken on a platform shaker
788 for 25 minutes at 200 rpm. Then, we transferred the fixed embryos to 2 ml microfuge tubes, sequentially
789 added n-heptane and 90% ethanol in equal proportions, vigorously shook for ~30 sec to remove the vitelline
790 membrane, and washed 3x with 90% ethanol. We started the staining immediately after (though storage in
791 90% ethanol possible for ~1 week). The embryos were rehydrated with PBT (3 washes), stained with 1:1000
792 DAPI for 1 hour, 1:500 Phallacidin for 1-hour, washed 4x with PBT, re-suspended in 3:1 glycerol:PBS solution,
793 and mounted between 2 rectangular coverslips for imaging. Images were acquired on Leica SP8 DMi8
794 inverted confocal microscope using 20x/0.75 NA glycerol objective, 1.2x digital zoom, 1 µm z-step, and 0.473
795 µm/pixel x-y resolution.

796 Image analysis and statistics: All image analysis was performed in FIJI. We conducted 11 types of analyses in
797 live or fixed embryos: 1) Germband extension (live), 2) developmental landmarks analysis (live) 3) whole
798 embryo reconstruction of nuclear distribution (fixed), 4) nuclear expulsions (live), 5) nuclear movements
799 (live), 6) nuclear cycle asynchrony (live), 7) nuclear crowding (live), 8) fraction of mitotic failures (live), 9) SLBP
800 nuclear localization (live), 10) F-actin and microtubule distribution (live), and 11) comparing the distribution
801 of nuclei and F-actin (fixed). All the statistical analysis were performed in Prism (GraphPad), including curve
802 fitting (see below, nuclear crowding, SLBP localization, and F-actin and microtubule distribution), non-
803 parametric tests (non-parametric Kruskal-Wallis test with Dunn's uncorrected test for multiple comparisons),
804 and estimating the 95% confidence intervals (CI) on the medians. The straight-line fits for analysis of nuclear
805 movements were done using the curve fitting functions in ImageJ macro language.

806 For **Germband extension** (GBE), we measured the distance of the anterior end of the posterior mid-gut
807 (PMG) from the embryo posterior end. The GBE was calculated as,

808 $$percent\ GBE = \frac{distance\ of\ PMG\ from\ posterior * 100}{length\ of\ the\ embryo}$$

809 Plotting percent GBE against time shows the fast and slow phases of GBE.

810 For **developmental landmarks analysis,** we noted down the time at which following developmental stages
811 occurred. For *40% GBE*, we noted down the time when the anterior tip of the PMG was closest to 40% embryo

812 length from the posterior pole. For *Germband retraction begins* and *ends*, we noted down the time when the
813 anterior tip of the elongated ectoderm on the dorsal side first moved towards the posterior and then
814 stopped. For *head involution*, we noted down the time when the ectoderm meets in the anterior.

815 For **whole embryo reconstruction of nuclear distribution**, we used a custom-built image analysis pipeline to
816 fuse the two views of the embryo, and visualize subcortical nuclei; either isolated or in clusters. We refer to
817 each view as "half embryo", even though each spans about 70-75% of the embryo width, providing a
818 substantial overlap. The pipeline comprises, as outlined in the following, elements in FIJI for processing the
819 raw images, stitching the two halves, rendering a dorsal-ventral view, segmenting the embryo volume, and
820 then color-coding the nuclei by distance from the segmented embryo surface. We first processed the raw
821 images to improve visualization of the nuclei ('Minimum 3D' filter, radii x=y=1, z=3; then 'Median 3D' filter,
822 radii x=y=z=1). Then, we homogenized the brightness/contrast between the two half embryos. We then
823 manually aligned the halves along their AP axis and used the BigWarp[71] within BigDataViewer[72] to register
824 them using manually selected interest points (subcortical- or yolk-nuclei) visible in both halves. We tightly
825 cropped the output images to reduce the computational load in the steps to follow. Then, we used
826 BigStitcher[73] to further align the embryo, using the phase correlation method, to produce the "fused
827 embryo". In the case of many embryos, additional manual transforms were necessary to obtain an acceptable
828 fused embryo. The fused embryos were rotated and resliced to produce dorsal-ventral views. We then used
829 thresholding on nuclear signal to segment embryo volume, generating a binary embryo mask, and used '3D
830 Distance Map' (from '3DSuite' in ImageJ[74]) to compute the Euclidian distances from embryo surface for each
831 voxel inside the embryo. Voxels with distance <18 µm were classified as cortical, 18-45 µm as subcortical,
832 and >45µm as yolk region (Figure 2B); these distances were determined empirically, using measurements
833 from various fused embryos. The regions were then color-coded and presented as maximum projections and
834 cross-sections in Figure 2. For embryos with a blastoderm hole, we further localized the hole in the embryo
835 coordinates, and mapped these locations from multiple embryos onto a model embryo surface. The
836 maximum intensity projections of the dorsal and ventral halves of the model embryo show that the
837 blastoderm holes predominantly occur in the central region of the embryo.

838 For **nuclear expulsions**, we tracked expelled nuclei back in time to identify the mitosis when they were born
839 and to categorize the expulsion as isolated (Figure 4A, B) or pairwise (Figure 4E). A nucleus was defined as
840 expelled if its apical tip lay ≥12 µm away from the embryo surface. To simplify the identification of expelled
841 nuclei, we color-coded the Histone-RFP signal as a function of distance from embryo surface. This is similar
842 to above analyses, except we use the 'LocalZPojector' plugin[75] in FIJI, with embryo surface inferred from the
843 co-imaged Jupiter-GFP signal. After color-coding the nuclei, we manually identify and count the number of
844 pairwise or isolated nuclear expulsions.

845 For **nuclear movements**, we manually tracked the entire lineage for select few nuclei from the mother
846 nucleus in late interphase 10 to all 8 great-granddaughter nuclei in late interphase 13. Nuclei from a single
847 lineage were treated as a single "group", yielding a group center at each time point. We chose nuclei along
848 one continuous row at interphase 10 and only chose those groups whose entire progeny (all 8 great-
849 granddaughters) could be tracked, yielding ≥13 groups per embryo. For each group, we fitted a straight line
850 to the time series of the group-center coordinates (dashed lines in Figure 5B) to capture the global drift, and
851 then computed, at every time point, the distance of the group-center to this line. An average of these
852 distances during a specific period was used to estimate of group-center deviations over that period. Since
853 the groups move strongly from anaphase through the first few minutes of the subsequent interphase, we
854 analyzed "extensive-movement" and "low-movement" periods separately. Extensive movements
855 consistently began ≥1 timepoint (30 s) before the first telophase appeared in any tracked groups and largely
856 subsided within 3 minutes after all groups completed telophase. Thus, we defined the extensive-movement

857 window as 30 s before the first telophase nuclei to 3 min after the last telophase nuclei. With these
858 objectively defined windows, average group-center deviations were straightforward to compute. Then, at
859 29°C, we further followed the progeny of the 8 great-granddaughter nuclei to identify those nuclear groups
860 that have at least one mitotic failure during mitosis 13, leading to pair-wise nuclear expulsions in interphase
861 14.

862 For **nuclear cycle asynchrony**, we marked key time points in the timelapse recordings to follow nuclear cycle
863 progression in the anterior-, middle-, and posterior-5th of the field of view. We focused on the transitions
864 from a telophase 13 to interphase 14. If these timepoints are 'T_a' (anterior), 'T_p' (posterior), and 'T_m' (middle),
865 the 'asynchrony' can be calculated as,

866 $$asynchrony = T_m - \left(\frac{T_a + T_p}{2}\right)$$

867 Thus, we assume that in a fully synchronous embryo T_m equals the average of T_a and T_p; deviation from this
868 expected value quantifies asynchrony.

869 For **nuclear crowding**, we analyzed nuclear distribution at the end of interphases, when the distribution is
870 stable and crowding is maximal, if any. We first segmented the nuclei using 'Find Maxima' to detect local
871 intensity peaks, generating an image of maxima. These maxima were then manually curated: we removed
872 the maxima not corresponding to nuclei, add missing ones, and corrected the maxima that were clearly off-
873 center. Then we used Voronoi tessellation to mark territories (pseudo-cells) around each nucleus. We
874 excluded territories that (1) touched the edge of the image, (2) had aberrant shapes (aspect ratio>2), or (3)
875 contained pixels with <5 units of intensity (typically poorly defined pseudo-cells at the edge of segmentation).
876 Each nucleus was thus associated with a pseudo-cell area ('Area', μm^2) and the x-coordinate of the pseudo-
877 cell center ('X', µm) with x-axis aligned the embryonic AP axis. We then fitted a parabola to the Area-X
878 relationship,

879 $$Area = aX^2 + bX + c$$

880 Greater nuclear crowding corresponds to stronger curvature (compare Figure 6I-L); therefore, the fit
881 parameter 'a', which dictates the curvature, was used a quantitative measure of crowding.

882 For **fraction of mitotic failures**, we tracked expelled nuclei back in time (see above nuclear expulsion), but
883 additionally recorded their positions, to map where mitotic failures occurred within the field-of-view. In
884 parallel, we generated regions of (1) maximum nuclear crowding, (2) maximum delay in nuclear divisions,
885 and (3) their combination. To construct <u>crowded regions</u>, we drew on previous studies showing that syncytial
886 divisions arrest when a threshold nuclear content is reached at ~70% of the normal cellularization nuclear
887 density[26–29]. A previous study reported the nuclear domain (pseudo-cell) area to be 28.8 μm^2 at
888 cellularization[76], which we corroborated (data not shown). For simplicity, we assumed 6000 nuclei at
889 interphase 14, each with an area of 29 μm^2. At 70% density, this corresponds to 4200 nuclei with area 41.43
890 μm^2, approximated as 42 μm^2. Thus, we estimated that divisions should arrest when pseudo-cell area falls
891 below ~42 μm^2. At 29°C, many nuclei in the central regions had areas <42 μm^2 in interphase 13, so we used
892 this criterion to define regions likely to have reached the 70% density one division earlier, locally. At normal
893 temperatures (22, 25, and 28°C), nuclei rarely had areas <42 μm^2; therefore, we defined crowded regions as
894 nuclei in the lower quartile of the pseudo-cell areas. This construction is a practical rationalization and not a
895 mechanistic statement about how the effect of nuclear crowding might manifest. Then, to define <u>delayed</u>
896 <u>region</u> (maximally delayed nuclear divisions), we marked the areas containing the last ~20% of the nuclei to
897 complete nuclear cycle 13. This empirically chosen fraction yielded regions similar in size as the crowded
898 regions. The rationale, based on previous work[25], is that division control is coordinated at the embryo scale,

899 and shared cytoplasm implies that locally delayed cycles will conflict with the embryo-wide biochemical
900 status. Finally, we obtained the combined region using the logical OR operator of crowded and delayed
901 regions, to test the combinatorial effects of crowding and asynchrony. In the end, for each embryo we
902 computed the fraction of mitotic failures in each region as,

903 $$fraction\ of\ mitotic\ failures = \frac{number\ of\ mitotic\ failures\ in\ a\ specific\ region}{total\ number\ of\ mitotic\ failures}$$

904 As we can imagine, the fraction of mitotic failures will also depend on the size of the specific region, as
905 compared to the total field of view. As such, in case of both crowded and delayed regions, we empirically
906 determined criteria for their construction, such that the size of these regions will be comparable: ~20% of
907 the field of view. In case of combined regions, however, the size can vary from ~20% (crowded and delayed
908 regions show complete overlap) to ~40% (crowded and delayed regions show no overlap).

909 There was a marginal increase in embryo lethality at 25°C in the controls for the overexpression experiments,
910 which presumably happens due to the presence of additional transgenic insertions (UAS and Gal4). Due to
911 this reason, to err on the side of caution, we chose to perform the imaging at 22°C, specifically for the Fraction
912 of mitotic failures analysis. As such we don't expect any biologically significant difference between results at
913 22°C and 25°C terms of in embryo lethality, blastoderm holes, or other defects.

914 For **SLBP nuclear localization**, we tracked nuclei from late interphase 13 till early interphase 14 in embryos
915 expressing GFP-tagged SLBP and Histone-RFP, developing at 25°C or 29°C. To measure the nuclear SLBP
916 intensity, we drew ROIs (3 µm diameter) in the center of the nuclei in RFP channel, applying these ROIs to
917 GFP channel. The same procedure was applied to embryos expressing GFP-tagged SLBP.S118A or NLS, along
918 with Histone-RFP, to compare localization kinetics. After identifying the two components of SLBP loss during
919 interphase 14 in nuclei with mitotic failure during mitosis 13, we fitted a straight line to nuclear intensities
920 between 0 and 4 minutes of interphase 14.

921 For **F-actin and microtubule distribution**, we tracked F-actin caps and microtubule spindles around the same
922 nuclei during mitosis 13 (late prophase to end of metaphase) in embryos developing at 25°C or 29°C, and
923 followed the divisions to classify them as normal or mitotic failures. For F-actin caps, we manually outlined
924 the cap and fitted an ellipse to this contour to obtain cross-sectional area, aspect ratio, and the orientation
925 of the major axis. For microtubule spindles, we manually drew a line between spindle poles to measure the
926 spindle length and the spindle-axis orientation. These measurements were used to plot F-actin cap area and
927 aspect ratio at metaphase, spindle length at metaphase, and the relative angle between cap long axis and
928 spindle axis. Cumulative spindle rotation was computed as the sum of absolute angular changes between
929 consecutive time points. The rate of spindle-length change was estimated as a linear-fit to spindle length
930 over time across mitosis.

931 For **comparing the distribution of nuclei and F-actin**, we used a pipeline similar to that for 'whole embryo
932 reconstruction of nuclear distribution', but without fusing two half-embryos and starting directly from
933 embryo-volume segmentation using the F-actin staining. A 3D distance map was then computed and nuclei
934 classified into cortical, subcortical, or yolk based on their distance from the embryo surface. These nuclei
935 were color-coded and presented as sum projections in Figure S6 (except for yolk region).

936 Analysis of thermoclinal genes: We sought genes showing variation across natural populations of *Drosophila*
937 *melanogaster* along large-scale climatic gradients. At continental scale, we reasoned that climatic variation
938 imposes selection gradient with distance from equator, generating geographic genomic variation, i.e., a
939 thermocline, across a temperature range of at least 15°C. Previous studies reported such variation at
940 different scales (whole genome, Quantitative Trait Loci, or individual genes/proteins, see Table S1 for the list

941 of studies). To be able to aggregate over these scales we chose "genes" as a level of abstraction.
942 Consequently, we focus our analysis to genes that show consistent clinality across data sets, rather than to
943 specific allelic change (coding vs. non-coding, position in the protein, etc.) that are involved. We thus
944 extracted only genes reported to vary across geographically distant populations, and grouped studies by
945 continent (North America, Europe, or Australasia), assuming these continent-scale gradients arose
946 independently. The resulting "thermoclinal datasets" were then used to assign a score of 0 to 3 for a gene,
947 counting the number of appearances in individual datasets.

948 To assemble genes relevant for spindle dynamics, we combined the genes associated with Gene Ontology
949 (GO) terms cell polarity, spindle localization, and spindle organization; none of the individual GO terms alone
950 capture all six candidate genes tested in this study. We queried the thermoclinal datasets with this combined
951 list of genes related to spindle dynamics, assigning each gene a 0 to 3 score as above. For comparison, we
952 applied the same procedure to genes associated with GO term 'metabolic process'. See also, Tables S1 and
953 S2.

954 **Figure and table legends:**

955 **Figure 1: Embryonic lethality and developmental defects in embryos exposed to elevated temperature.**

956 (A, B) To assess developmental robustness, we exposed embryos to various temperature regimes and
957 estimated the embryo lethality. (A) Schematic showing the temperature regimes in the embryo survival
958 experiment. Here we have three conditions depending on exposure to normal or elevated temperature
959 regimen in the 3-hour time windows as shown, normal-normal [NN], elevated-normal [EN], and normal-
960 elevated [NE]. In all cases, the first time-window also includes 1 hour of embryo collection. Embryonic
961 development beyond 6 hours continued at normal temperature. (B) The scatter plots show the distribution
962 of the percentage of embryos that don't hatch into larvae. Each dot represents data from a sample with ≥26
963 embryos; n= 12 (NN), 10 (EN), 10 (NE) samples.

964 (C-E) Montages show embryos, expressing Histone-RFP, from early gastrulation till late gastrulation, in
965 embryos at 25°C. Till late cellularization stage, these embryos were exposed to either 25°C, i.e., NN
966 temperature regimen (C), or 29°C, i.e., EN temperature regimen, showing mild (D), or severe (E) defect. White
967 dashed lines, dorsal midline drawn based on the egg shape; red dashed lines, the embryonic midline in the
968 dorsal posterior ectoderm; orange dashed lines, anterior end of the posterior mid-gut (extent of GBE).

969 (F) Plot show extent of GBE: hollow markers, embryos with gastrulation defects, which are excluded from
970 further analysis of developmental landmarks. (G) The analysis of Developmental landmarks shows the time
971 at which various events can be seen in the embryos. Time points from individual embryos are plotted at the
972 same y-value.

973 Scale bar, 50 µm. B show scatters with median, with whiskers showing 95% CI. Non-parametric Kruskal-Wallis
974 test with Dunn's uncorrected test for multiple comparisons: *, $p<0.05$; **, $p<0.01$; ***, $p<0.001$; ****,
975 $p<0.0001$, non-significant comparisons are not shown.

976 **Figure 2: Nuclear loss lacks left-right symmetry in embryos developing at elevated temperature.**

977 (A) Pie charts show occurrence of blastoderm holes during cellularization in fixed embryos at normal
978 temperature (n=68) or elevated temperature (n=77): blastoderm hole, a cluster of >10 subcortical nuclei with
979 a corresponding discontinuity in the cortical layer.

980 (B) Schematic shows various layers of the embryo volume: green, cortical nuclei, <18 µm from embryo
981 surface; magenta, sub-cortical nuclei, >18 µm and <45 µm from embryo surface; yellow, yolk nuclei
982 (vitellophages), >45 µm from embryo surface.

983 (C-H) Distribution of nuclei in embryos during mid-cellularization (interphase 14), in fixed embryos that were
984 developing at normal temperature (C, F) or elevated temperature that shows either a mild defect (D, G) or a
985 severe defect (E, H). Top/bottom panels, maximum intensity projections in dorsal/ventral halves of the
986 embryos; white/grey dashed lines, midlines drawn based on the egg shape. The voxels are color-coded as in
987 B. Embryo orientation is consistently presented in all panels and is indicated in C. (C-E) Cortical and
988 subcortical nuclei are shown. Embryos at normal temperature (C) show rarely any gaps, while those at
989 elevated temperature occasionally show small gaps (D) or blastoderm holes (E), indicating discontinuities in
990 the distribution of cortical nuclei, corresponding also with the locations of subcortical nuclei. (F-H) The
991 corresponding subcortical nuclei are shown separately for improved visibility, along with yolk nuclei.

992 (I-N) Cross-sectional views long the orange and cyan dashed lines in C-H. Embryo orientation is consistently
993 presented in all panels and is indicated in I.

994 (O, P) Blastoderm holes from 11 embryos at elevated temperature were mapped onto a model embryo
995 surface (one blastoderm hole per embryo). Images show projections in dorsal (O) and ventral (P) halves of
996 the model embryo. *, blastoderm hole from embryo in E/H.

997 Scale bars: F, 50 µm; I, 25 µm.

998 **Figure 3: Cortical nuclei are expelled in embryos at elevated temperature.**

999 (A-E) Montages showing live embryos, expressing Histone-RFP, from early interphase 10 till late interphase
1000 14, developing either at 22°C (A), 25°C (B), 28°C (C), or at 29°C showing mild (D), or severe (E) defect. The
1001 nuclei were labelled as a function of their distance from the embryo surface. Green, cortical nuclei; magenta,
1002 sub-cortical nuclei that are lost (see also schematic in Figure 4B). At elevated temperature, a lot more nuclei
1003 are expelled, and as a result, we can see gaps between cortical nuclei, coinciding with subcortical nuclei:
1004 arrowheads, small gaps; arrows, blastoderm hole.

1005 Scale bar, 25 µm.

1006 **Figure 4: Nuclear loss as isolated or paired expulsions at elevated temperature.**

1007 Following isolated nuclear expulsions back in time, we found them to stem from both out-of-plane and in-
1008 plane divisions. (A) Montages exemplify out-of-plane division during mitosis 10 at 25°C. Histone-RFP marks
1009 nuclei (green), Jupiter-GFP marks microtubules (magenta). Arrowheads, in-plane divisions; arrows, out-of-
1010 plane division; white lines, embryo surface. Each subsequent frame is 1 minute apart. (B) Montage
1011 exemplifies in-plane divisions at 25°C, from telophase 12 to interphase 13. Histone-RFP marks nuclei: cortical
1012 nuclei, green; subcortical nuclei, magenta; see schematic. The arrowheads/arrows track the daughter nucleus
1013 that will be expelled/cortically retained. Inset, time since telophase 12. (C, D) Scatter plots show number of
1014 out-of-plane divisions during mitosis 10 (C) and number of isolated nuclear expulsions during interphase 14.

1015 To assess the pairwise loss of nuclei, we counted mitotic failures. (E) Montage exemplifies mitotic failure at
1016 29°C, from late interphase 12 to late interphase 13. Histone-RFP marks nuclei: cortical nuclei, green;
1017 subcortical (lost) nuclei, magenta; see the schematic in B. White arrows, normal nuclear division; white
1018 arrowheads, mitotic failure; cyan arrowheads, lagging chromosomes. Inset, time since telophase 12. (F)
1019 Scatter plot shows number of mitotic failures during interphase 14. (G) The schematic illustrates the
1020 phenomenon of mitotic failures at elevated temperature.

1021 Scale bars: A, 10 µm; B and E, 5 µm. C, D, and F show scatters with median, with whiskers showing 95% CI.
1022 Large hollow markers, embryos with blastoderm holes; small hollow markers, embryos with small gaps in the
1023 blastoderm. n= 10 (22°C), 7 (25°C), 9 (28°C), and 10 (29°C) embryos. Non-parametric Kruskal-Wallis test with

1024 Dunn's uncorrected test for multiple comparisons: *, p<0.05; **, p<0.01; non-significant comparisons are not
1025 shown.

1026 **Figure 5: Nuclear movement parallel to the embryo surface is amplified at elevated temperature.**

1027 (A-C) An example of nuclear movement tracking. Snapshots from embryo at 29°C, with Histone-RFP marking
1028 nuclei, showing the mother nuclei at the end of interphase 10 (A) and the corresponding 8 great-
1029 granddaughter nuclei, each, at the end of interphase 13 (C), connected via the group-center trajectories (B).
1030 Cyan and yellow, neighbouring nuclear groups; thickening solid lines, trajectories of group-centers with
1031 increasing number of nuclei due to divisions; dotted lines, linear fits to group-center trajectories; shaded
1032 region, periods of greatest movement (see methods).

1033 (D-I) To quantify the drift in the nuclear group centers, we compute the slope of the linear fits (dotted lines
1034 in B). Plots show the distribution of embryo medians, for the drift along the AP axis (D) and DV axis (E). To
1035 quantify the movements in nuclear group centers during interphase-metaphase vs. anaphase-telophase
1036 (shaded vs. unshaded region in B), we compute the average of the deviations from the linear fits. Plots show
1037 the distribution of embryo medians, for the fluctuations along the AP axis (F, H) and DV axis (G, I), during
1038 interphase-metaphase (F, G) and anaphase-telophase (H, I). Large hollow markers, embryos with blastoderm
1039 holes; small hollow markers, embryos with small gaps in the blastoderm. n= 10 (22°C), 7 (25°C), 9 (28°C), and
1040 10 (29°C) embryos.

1041 (J) To test whether nuclear groups with highest movement also correspond to mitotic failures, we plot the
1042 deviations along AP-axis, now showing all of the tracked nuclear groups at 29°C. Hollow markers, nuclear
1043 groups with at least one subsequent mitotic failure; underlined, embryo with blastoderm holes; insets,
1044 number of tracked nuclear groups.

1045 Scale bar, 25 µm. D to J show scatters with median, with whiskers showing 95% CI. Non-parametric Kruskal-
1046 Wallis test with Dunn's uncorrected test for multiple comparisons: *, p<0.05; **, p<0.01; ***, p<0.001; non-
1047 significant comparisons are not shown, statistical tests not performed on data in J.

1048 **Figure 6: Nuclear crowding and Nuclear cycle asynchrony increase at elevated temperature.**

1049 To assess the crowding of nuclei, we segmented the nuclei and generated pseudo-cells. (A-D) Snapshots from
1050 embryos at the end of interphase 13 at indicated temperatures: Histone-RFP marks the nuclei; outline, region
1051 of the image considered for quantifications. (E-H) The pseudo-cells for the corresponding embryos in A-D.
1052 Color indicates pseudo-cell area in μm^2, LUT at the bottom. (I-L) Plots show distribution of pseudo-cell areas
1053 as a function of AP position embryos in A-D. Dotted line, quadratic fit. (M) Scatter plots show distribution of
1054 the coefficient of the quadratic term, with a larger quadratic coefficient indicating greater crowding. (N) The
1055 schematic illustrates the crowding effect at elevated temperature: size of the black arrows, gradation in
1056 nuclear density.

1057 To assess the asynchrony in nuclear cycles, we identified the phases of the nuclear cycle along the AP axis.
1058 (O, P) Image shows the entire anterior-posterior extent of the field of view, from embryos at 25°C (O) and
1059 29°C (P). Histone-RFP marks the nuclei: green, cortical nuclei; magenta, subcortical (lost) nuclei (see also
1060 schematic in Figure 4B). Arrows show the direction in which the wave of the nuclear division cycle will
1061 progress. At 25°C, we see a single wave from the anterior, while at 29°C we see an anterior- and a posterior-
1062 wave. (Q) Scatter plots show asynchrony in initiation of interphase 14. (R) The schematic illustrates the
1063 progressive increase in asynchrony at elevated temperature.

1064 Scale bars, 20 µm. M and Q shows scatters with median, with whiskers showing 95% CI. Large hollow markers,
1065 embryos with blastoderm holes; small hollow markers, embryos with small gaps in the blastoderm. n= 10

1066 (22°C), 7 (25°C), 9 (28°C), and 10 (29°C) embryos. Non-parametric Kruskal-Wallis test with Dunn's uncorrected
1067 test for multiple comparisons: *, p<0.05; **, p<0.01; ***, p<0.001; non-significant comparisons are not
1068 shown.

1069 **Figure 7: Nuclear crowding and nuclear cycle asynchrony combinatorially enhance mitotic failures.**

1070 (A, B) Snapshots from embryos at 29°C, at the end of interphase 13 (A) and 14 min afterwards (B). Histone-
1071 RFP marks nuclei; green outline, region of the image with nuclear crowding; magenta outline, region
1072 containing the most delayed nuclei, i.e., those that are most lagging in nuclear division cycles.

1073 (C-E) The locations of lost pairs of nuclei during interphase 14 (mitotic failures during mitosis 13) are marked
1074 as white dots. Then, various regions are defined in the embryo to illustrate the fraction of mitotic failures
1075 occurring in that region. These regions are composed based on, the crowded region (C), the delayed region
1076 (D), and the combined region (E).

1077 (F-K) Scatter plots show distribution of the fraction of mitotic failures occurring in the crowded (F), delayed
1078 (G), and combined (H) regions of the embryos, and the distribution of the area fractions in crowded (I),
1079 delayed (J), and combined (K) regions of the embryos. In the case of the area fraction of the combined regions
1080 (K), the increase in the overlap of crowded and delayed regions reduces the overall size of the combined
1081 regions.

1082 Scale bars, 20 µm. F-K show scatters with median, with whiskers showing 95% CI. Large hollow markers,
1083 embryos with blastoderm holes; small hollow markers, embryos with small gaps in the blastoderm. n= 10
1084 (22°C), 7 (25°C), 9 (28°C), and 10 (29°C) embryos. Non-parametric Kruskal-Wallis test with Dunn's uncorrected
1085 test for multiple comparisons: *, p<0.05; **, p<0.01; ***, p<0.001; non-significant comparisons are not
1086 shown, significance not tested for I and J (see methods).

1087 **Figure 8: Mitotic failures lead to DNA damage response.**

1088 (A) Schematic shows how the mislocalization of the Stem-Loop Binding Protein (SLBP) can be used as a
1089 reporter for DNA damage. During interphase, SLBP normally localizes to the nuclei, while it is excluded in
1090 nuclei with DNA damage.

1091 (B) The nuclear localization of SLBP (green) allows us to distinguish nuclei with DNA damage (dashed circles)
1092 vs. normal ones (circles). Following these nuclei over a mitosis shows that nuclei with DNA damage are
1093 mitotically arrested, while the normal nuclei divide, giving rise to two daughter nuclei (smaller circles). One
1094 of the nuclei with DNA damage is lost to embryo interior by the last timepoint. Inset: time since mitosis.

1095 (C-E) Montages show representative embryos developing at 29°C from telophase 13 till early interphase 14,
1096 in embryos expressing SLBP-GFP (C), SLBP.S118A-GFP (D), and NLS-GFP (E). Arrows, chromosome segregation
1097 defect; asterisks, pair of defective daughter nuclei; dashed circles, reduction in GFP-signal in the nuclei with
1098 mitotic failure, still localized cortically; inset, time since beginning of interphase 14.

1099 (F-K) Quantifications showing the kinetics of nuclear localization of SLBP-GFP (F), SLBP.S118A-GFP (G), and
1100 NLS-GFP (H) in control divisions in embryos at 25°C, control division in embryos at 29°C, and mitotic failures
1101 in embryos at 29°C. Slope of a straight-line fit between timepoints 0 to 4 min in F-H is plotted respectively (I-
1102 K). Insets, the number of embryos (N) used for pooling the number of nuclear divisions (n).

1103 Scale bars; B, 10 µm; C, 5 µm. F-H plots median values over time, with shaded regions showing 95% CI. I-K
1104 show scatters with median, with whiskers showing 95% CI. Non-parametric Kruskal-Wallis test with Dunn's
1105 uncorrected test for multiple comparisons: ***, p<0.001; non-significant comparisons are not shown.

1106 **Figure 9: Weakened interaction between F-actin and microtubules precedes mitotic failures.**

1107 (A) Schematic depicts dramatic reorganisation of F-actin, microtubules, and chromatin as the nuclei transition
1108 from prophase to late metaphase (left). The images are then manually annotated (center) to facilitate
1109 automated quantitative analysis of F-actin caps and microtubule spindles (right).

1110 (B-E) Montages from representative control nuclear divisions (B, C) and mitotic failures (D, E) from embryos
1111 developing at 25°C (B, D) and 29°C (C, E), during mitosis 13. Left panels show montage of UtrABD- and Jupiter-
1112 GFP signal: dashed contour, manually outlined F-actin cap; white dots, manually marked spindle poles. Right
1113 panels show montage of corresponding Histone-RFP signal: dashed green line, long axis of F-actin cap; solid
1114 cyan line, spindle position; insets, time till end of metaphase.

1115 (F-K) Quantifications showing F-actin cap size (F) and aspect ratio (G) at metaphase, microtubule spindle
1116 length at metaphase (H), spindle extension rate (I) and cumulative rotation (J) during mitosis, and the angle
1117 mismatch between spindle axis and cap long-axis (K). n= 27 (25°C control division), 27 (29°C control division),
1118 10 (25°C mitotic failure), 15 (29°C mitotic failure) nuclei, pooled from N= 9 (25°C) and 9 (29°C) embryos.

1119 Scale bar, 5 µm. F-K show scatters with median, with whiskers showing 95% CI. Non-parametric Kruskal-Wallis
1120 test with Dunn's uncorrected test for multiple comparisons: *, p<0.05; **, p<0.01; ***, p<0.001; ****,
1121 p<0.0001; non-significant comparisons are not shown.

1122 **Figure 10: Rescue of embryonic lethality at elevated temperature through overexpressions, and clinal**
1123 **genes as "natural" candidates.**

1124 (A) Testing the rescue of embryonic lethality and the fraction of mitotic failures with overexpression of *αCat*
1125 or *sgg*. Scatter plot shows distribution of percent lethality in embryos from various genotypes, at normal
1126 (25°C) vs elevated temperature (29°C), calculated based on the fraction of embryos that don't hatch into
1127 larvae. Each dot represents data from a sample with ≥18 embryos: control, n= 10 (25°C), 11 (29°C) samples;
1128 αCat-OE, n= 10 (25°C), 12 (29°C) samples; sgg-OE, n= 8 (25°C), 7 (29°C) samples.

1129 (B-C) Scatter plots show distribution of the fraction of mitotic failures in crowded regions (B), and in combined
1130 regions (C), in the embryos at normal (22°C) vs elevated temperature (29°C). Each dot represents data from
1131 one embryo: control, n= 8 (22°C), 9 (29°C) embryos; αCat-OE, n= 8 (22°C), 8 (29°C) embryos; sgg-OE, n= 7
1132 (22°C), 7 (29°C) embryos.

1133 (D, E) Analysis of "natural" candidate genes that vary along thermoclines. (D) Venn diagram illustrates how
1134 we constructed a non-redundant list of genes associated with 'spindle dynamics' through the union of genes
1135 associated with GO terms, cell polarity (n=203 genes), spindle localization (n=37 genes), and spindle
1136 organization (n=138 genes). (E) Pie charts show clinal distribution scores for various genes associated with
1137 'spindle dynamics' as constructed in D (n=320 genes), or with GO term 'metabolic process' (n=6612 genes).
1138 ~1% of genes associated with 'spindle dynamics', while ~0.2% of the genes associated with 'metabolic
1139 process', are clinal in all three continental datasets. See also, Tables S1 and S2.

1140 A-C shows scatters with median, with whiskers showing 95% CI. In B and C, large hollow markers, embryos
1141 with blastoderm holes; small hollow markers, embryos with small gaps in the blastoderm. Non-parametric
1142 Kruskal-Wallis test with Dunn's uncorrected test for multiple comparisons: *, p<0.05; **, p<0.01; ***,
1143 p<0.001; ****, p<0.0001; non-significant comparisons are not shown.

1144 **Figure S1: Blastoderm holes appear in a fraction of embryos at elevated temperature.**

1145 The figure shows the snapshots from live embryos, expressing Histone-RFP, from early interphase 14, in
1146 embryos at elevated temperature (29°C). The nuclei are labelled as a function of their distance from the
1147 embryo surface. Here, green indicates cortical, and magenta indicates sub-cortical nuclei that are expelled
1148 (see also schematic in Figure 4B), while arrows/arrowheads indicate large/small blastoderm holes. For

1149 embryos with large blastoderm holes (embryos 05, and 08), we see many nuclei in magenta. In contrast, in
1150 the case of embryos with small blastoderm holes (embryos 04, and 09), we can see only a few nuclei in
1151 magenta per hole. We would argue that development in *Drosophila* is robust enough to buffer the defects
1152 due to the small gaps in the blastoderm, but fails at 29°C when large holes appear.

1153 Scale bar, 25 µm.

1154 **Figure S2: Defective nuclei take different amounts of time to be expelled from the embryo cortex.**

1155 (A, B) Montages from live embryos, with a few representative nuclei tracked from late interphase 12 to
1156 interphase 13. Top panels, Histone-RFP signal marking nuclei; bottom panels, Jupiter-GFP signal marking
1157 microtubules. Nuclei tagged in green/magenta are the ones that arise from mitotic defects during mitosis
1158 10/11. All of these are expelled during interphase 13. Notice the lack of spindle formation around the tagged
1159 nuclei. Also, note that the nuclei expelled by the 5th timepoint are not shown in the 6th timepoint. (A) An
1160 embryo developing at normal temperature (22°C), where 1 magenta and 1 green nuclei are followed. (B) An
1161 embryo developing at elevated temperature (29°C), where 6 magenta and 3 green nuclei are followed.

1162 Scale bars, 20 µm. Insets, time in min:sec.

1163 **Figure S3: Nuclear movement along surface-yolk axis is amplified at elevated temperature.**

1164 Cross-sections from live embryos, expressing Histone-RFP, from late interphase 13 till early interphase 14, in
1165 embryos developing either at normal temperature (22°C, A) or at elevated temperature (29°C, B). Colored
1166 lines, basal tip of nuclei in the first frame; insets, time since initiation of anaphase 13 at the left/right extreme
1167 of the images (which is also the first time we see the shift from baseline in embryo at elevated temperature);
1168 arrowheads, local peak of the nuclear shift from the baseline; arrow, expelled nuclei.

1169 Scale bars, 25 µm. Cross-sections are in the lateral region of the embryos, anterior to the left.

1170 **Figure S4: Nuclear cycle asynchrony at elevated temperature during embryo development.**

1171 To assess the asynchrony in nuclear cycles, we identified the phases of the nuclear cycle along the AP axis.
1172 (A, B) Montages show the transition from nuclear cycle 13 to early interphase 14, from live embryos at 25°C
1173 (A), and at 29°C (B). Histone-RFP marks the nuclei: green, cortical nuclei; magenta, subcortical (lost) nuclei
1174 (see also schematic in Figure 4B); inset, time in min:sec. The anterior, central, and posterior 1/5th of the field
1175 of view are as indicated. Time 00:00 is when the anterior 1/5th of the embryo enters interphase 14. Boxes
1176 highlight entry into interphase 14 in that region.

1177 Scale bars, 20 µm.

1178 **Figure S5: Embryonic lethality at elevated temperature in *baz* or *dlg* overexpressions.**

1179 (A) Testing the rescue of embryonic lethality and the fraction of mitotic failures with overexpression of *baz*
1180 and *dlg*. Scatter plot shows distribution of percent lethality in embryos from various genotypes, at normal
1181 (25°C) vs elevated temperature (29°C), calculated based on the fraction of embryos that don't hatch into
1182 larvae. Each dot represents data from a sample with ≥12 embryos; control, n= 9 (25°C), 9 (29°C) samples;
1183 baz-OE, n= 11 (25°C), 10 (29°C) samples; dlg-OE, n= 12 (25°C), 10 (29°C) samples.

1184 (B, C) Scatter plots show distribution of the fraction of mitotic failures in crowded regions (B), and in
1185 combined regions (C), in the embryos at normal (22°C) vs elevated temperature (29°C). Each dot represents
1186 data from one embryo: control, n= 7 (22°C), 9 (29°C) embryos; baz-OE, n= 7 (22°C), 7 (29°C) embryos; dlg-OE,
1187 n= 6 (22°C), 7 (29°C) embryos.

1188 Plots show scatters with median, whiskers show 95% CI. In B and C, large hollow markers, embryos with
1189 blastoderm holes; small hollow markers, embryos with small gaps in the blastoderm. Non-parametric
1190 Kruskal-Wallis test with Dunn's uncorrected test for multiple comparisons: *, p<0.05; **, p<0.01; ***,
1191 p<0.001; non-significant comparisons are not shown.

1192 **Figure S6: Elevated temperature disrupts the association between nuclei and F-actin caps.**

1193 Distribution of nuclei and F-actin in embryos during interphase 13, in fixed embryos that were developing
1194 either at normal temperatures (A, C, D), or elevated temperature (B, E, F). (A, B) The images show SUM
1195 projections of the DAPI-stained nuclei (top image) and Phallacidin-stained F-actin (bottom image) of
1196 representative embryos. In the top images, the nuclei are labelled as a function of their distance from the
1197 embryo surface, where green indicates cortical, and magenta indicates sub-cortical nuclei (see also schematic
1198 in Figure 2B). The yolk nuclei are not shown. Anterior is on the left, dorsal up. (C-F) The top and bottom
1199 images show a zoomed-in view of the indicated regions in panels A and B. Arrowheads, expelled nuclei (C, E
1200 top panels) and corresponding gaps between the actin-caps (C, E bottom panels); arrows, gaps between
1201 neighbouring nuclei (D, F top panels) and corresponding gaps between the actin-caps at normal temperature
1202 (D, bottom panel) and "empty actin caps" at elevated temperature (F, bottom panel).

1203 Scale bars, 25µm. The boxed regions are 60x60 µm.

1204 **Figure S7: *mud* or *insc* overexpression does not ameliorate embryo survival at elevated temperature.**

1205 Scatter plot shows the distribution of percent lethality in embryos from various genotypes, at normal (25°C)
1206 vs elevated temperature (29°C), calculated based on the fraction of embryos that don't hatch into larvae.
1207 Each dot represents data from a sample with ≥21 embryos; control, n= 10 (22°C), 11 (29°C) samples; mud-
1208 OE, n= 11 (22°C), 12 (29°C) samples; insc-OE, n= 7 (22°C), 10 (29°C) samples. As we can see in the plot, neither
1209 *mud* nor *insc* overexpression rescues the embryo lethality at elevated temperature, with *mud* overexpression
1210 increasing embryo lethality even at normal temperature (25°C).

1211 The plot shows scatters with a median, while whiskers show 95% CI. Non-parametric Kruskal-Wallis test with
1212 Dunn's uncorrected test for multiple comparisons: *, p<0.05; **, p<0.01; ***, p<0.001; non-significant
1213 differences are omitted.

1214 **Table S1:** This table contains genes that are identified as being clinal in different continents. Columns A to C
1215 contain lists of studies, and under the studies is a list of genes that are identified in these studies as being
1216 clinal. Columns A, B, and C respectively list studies that have data from the continents of Australia and/or
1217 Australasia (AUS) [77–86], North and/or Central America (USA) [77,84,94–96,86–93], and Europe and/or North Africa (EU)
1218 [77,83,97,98]. We collect all the genes associated with 'spindle dynamics' (Figure 9D), to compile a list of potential
1219 candidate genes in Column F. For each gene in column F, we count the number of times that gene appears
1220 in columns A to C, counting a maximum of once per column, to respectively populate columns G to I. For each
1221 gene in column F, column J contains the sum of values in G, H, and I, to indicate the number of continents in
1222 which a gene is clinal. Each gene gets a score from 0 to 3, and we consider the gene to be a relevant candidate
1223 if it is found in at least 2 columns, i.e., with a score of 2 or 3.

1224 We collect all the genes associated with the GO term 'metabolic process', to compile a control list of
1225 candidate genes in Column L. For each gene in column L, we count the number of times that gene appears in
1226 columns A to C, counting a maximum of once per column, to respectively populate columns M to O. For each
1227 gene in column L, column P contains the sum of values in M, N, and O, to indicate the number of continents
1228 in which a gene is clinal. Thus, each gene gets a score from 0 to 3.

Table S2: Column A lists candidates from Table S1 column F that have a score of 2 or higher, i.e., those that show significant selectable variation in natural populations. For these genes, we query FlyBase (http://flybase.org/batchdownload) for additional details like gene name (column B), gene symbol (column C), and the level of expression during the first 2 hours of embryo development (column D). The level of expression is based on published transcriptomics data[99], and would correspond to a maternal pool of mRNAs, which is the most relevant mRNA source for this study. The candidate genes clinal in all 3 continents are highlighted in green. Columns F-J present a table with counts of genes that are associated with various categories of genes in Table S1 columns F and L, and a further breakdown of how many of these genes are clinal in how many continents. The breakdown is also plotted as pie charts in Figure 10E.

Table S3: This table lists various figure panels (columns A and B), and the related parental genotypes, i.e., the genotypes of females (column C) and males (column D) present in the embryo collection cages for the experiment related to a figure panel.

Additional information

Data and Code Availability: Data and codes developed for data analysis are available upon request from corresponding authors.

Author contributions: G.K. and S.L. planned the project. G.K. did the experiments with help from P.A. for baz and dlg overexpressions, JJ.D.-L. for co-staining of nuclei and F-actin. G.K. did the image analyses and statistical analyses. G.K. and S.L. wrote the manuscript, and all authors gave comments on the manuscript.

Acknowledgments: We would like to thank Lázaro Centanin, Nicolas Gompel, Marianthi Karageorgi, and Russ Hodge for insightful comments on various drafts of the manuscript, and Lemke lab members for discussions throughout the project. We are grateful to Jochen Wittbrodt for his enthusiasm and his continuous and generous support. We would also like to thank Ingrid Lohmann, Anja Nagel and Kristen Panfilio for *Drosophila* culture-related support, and Thomas Lecuit, Jan Felix Evers, and Eric Lecuyer for sharing fly lines. We sincerely appreciate the efforts taken by FlyBase to maintain a curated database and Bloomington Drosophila Stock Center for providing transgenic fly lines. This work was funded by the DFG (LE 2787/3-1) to S.L., while G.K. was supported through an HFSP Long-term postdoctoral fellowship (LT000597/2019-L).

Competing interests: The authors declare no competing financial interests.

References:

1. Wiens, J. J. Climate-Related Local Extinctions Are Already Widespread among Plant and Animal Species. *PLOS Biol.* **14**, e2001104 (2016).
2. Edwards, M. J. Review: Hyperthermia and fever during pregnancy. *Birth Defects Res. A. Clin. Mol. Teratol.* **76**, 507–16 (2006).
3. Miller, M. W. & Church, C. C. Arrhenius thermodynamics and birth defects: chemical teratogen synergy. Untested, testable, and projected relevance. *Birth Defects Res. C. Embryo Today* **99**, 50–60 (2013).
4. Graham, J. M. Update on the gestational effects of maternal hyperthermia. *Birth defects Res.* **112**, 943–952 (2020).
5. Cockroft, D. L. & New, D. A. T. Abnormalities induced in cultured rat embryos by hyperthermia. *Teratology* **17**, 277–283 (1978).
6. Germain, M. -A, Webster, W. S. & Edwards, M. J. Hyperthermia as a teratogen: parameters determining hyperthermia-induced head defects in the rat. *Teratology* **31**, 265–72 (1985).
7. Schirone, R. C. & Gross, L. Effect of temperature on early embryological development of the zebra fish, Brachydanio rerio. *J. Exp. Zool.* **169**, 43–52 (1968).

1272 8. Dorrity, M. W. *et al.* Proteostasis governs differential temperature sensitivity across embryonic cell
1273 types. *Cell* **186**, 5015-5027.e12 (2023).
1274 9. LILLIE, F. R. & KNOWLTON, F. P. ON THE EFFECT OF TEMPERATURE ON THE DEVELOPMENT OF
1275 ANIMALS. *Zool. Bull.* **1**, 179–193 (1897).
1276 10. Crapse, J. *et al.* Evaluating the Arrhenius equation for developmental processes. *Mol. Syst. Biol.* **17**,
1277 e9895 (2021).
1278 11. Kuntz, S. G. & Eisen, M. B. Drosophila embryogenesis scales uniformly across temperature in
1279 developmentally diverse species. *PLoS Genet.* **10**, e1004293 (2014).
1280 12. Chong, J., Amourda, C. & Saunders, T. E. Temporal development of Drosophila embryos is highly
1281 robust across a wide temperature range. *Interface* **15**, (2018).
1282 13. Welte, M. A., Tetrault, J. M., Dellavalle, R. P. & Lindquist, S. L. A new method for manipulating
1283 transgenes: engineering heat tolerance in a complex, multicellular organism. *Curr. Biol.* **3**, 842–853
1284 (1993).
1285 14. Foe, V. E. & Alberts, B. M. Studies of nuclear and cytoplasmic behaviour during the five mitotic
1286 cycles that precede gastrulation in Drosophila embryogenesis. *J. Cell Sci.* **61**, 31–70 (1983).
1287 15. Xie, Y. & Blankenship, J. T. Differentially-dimensioned furrow formation by zygotic gene expression
1288 and the MBT. *PLoS Genet.* **14**, e1007174 (2018).
1289 16. Mazumdar, A. & Mazumdar, M. How one becomes many: Blastoderm cellularization in Drosophila
1290 melanogaster. *BioEssays* **24**, 1012–1022 (2002).
1291 17. Martin, A. C. The Physical Mechanisms of Drosophila Gastrulation: Mesoderm and Endoderm
1292 Invagination. *Genetics* **214**, 543–560 (2020).
1293 18. Lecuit, T. & Yap, A. S. E-cadherin junctions as active mechanical integrators in tissue dynamics. *Nat.*
1294 *Cell Biol.* **17**, 533–539 (2015).
1295 19. Foe, V. E. Mitotic domains reveal early commitment of cells in Drosophila embryos. *Trends Genet.* **5**,
1296 322 (1989).
1297 20. Niemuth, J. & Wolf, R. Developmental asynchrony caused by steep temperature gradients does not
1298 impair pattern formation in the wasp, Pimpla turionellae L. *Roux's Arch. Dev. Biol.* **204**, 444–452
1299 (1995).
1300 21. Lucchetta, E. M., Lee, J. H., Fu, L. A., Patel, N. H. & Ismagilov, R. F. Dynamics of Drosophila embryonic
1301 patterning network perturbed in space and time using microfluidics. *Nature* **434**, 1134–1138 (2005).
1302 22. Deneke, V. E. *et al.* Self-Organized Nuclear Positioning Synchronizes the Cell Cycle in Drosophila
1303 Embryos. *Cell* **177**, 925-941.e17 (2019).
1304 23. Kanesaki, T., Edwards, C. M., Schwarz, U. S. & Grosshans, J. Dynamic ordering of nuclei in syncytial
1305 embryos: a quantitative analysis of the role of cytoskeletal networks. *Integr. Biol. (Camb).* **3**, 1112–9
1306 (2011).
1307 24. Schmidt, A. & Grosshans, J. Dynamics of cortical domains in early Drosophila development. *J. Cell*
1308 *Sci.* **131**, (2018).
1309 25. Deneke, V. E., Melbinger, A., Vergassola, M. & Di Talia, S. Waves of Cdk1 Activity in S Phase
1310 Synchronize the Cell Cycle in Drosophila Embryos. *Dev. Cell* **38**, 399–412 (2016).
1311 26. Edgar, B. A., Kiehle, C. P. & Schubiger, G. Cell cycle control by the nucleo-cytoplasmic ratio in early
1312 Drosophila development. *Cell* **44**, 365–72 (1986).
1313 27. Blythe, S. A. & Wieschaus, E. F. Zygotic genome activation triggers the DNA replication checkpoint at
1314 the midblastula transition. *Cell* **160**, 1169–1181 (2015).
1315 28. Lu, X., Li, J. M., Elemento, O., Tavazoie, S. & Wieschaus, E. F. Coupling of zygotic transcription to
1316 mitotic control at the Drosophila mid-blastula transition. *Development* **136**, 2101–10 (2009).
1317 29. Hayden, L. *et al.* Cullin-5 mutants reveal collective sensing of the nucleocytoplasmic ratio in
1318 Drosophila embryogenesis. *Curr. Biol.* **32**, 2084-2092.e4 (2022).
1319 30. Hayden, L., Hur, W., Vergassola, M. & Di Talia, S. Manipulating the nature of embryonic mitotic

1320 waves. *Curr. Biol.* **32**, 4989-4996.e3 (2022).
1321 31. Iampietro, C. *et al.* Developmentally Regulated Elimination of Damaged Nuclei Involves a Chk2-
1322 Dependent Mechanism of mRNA Nuclear Retention. *Dev. Cell* **29**, 468–481 (2014).
1323 32. Karr, T. L. & Alberts, B. M. Organization of the cytoskeleton in early Drosophila embryos. *J. Cell Biol.*
1324 **102**, 1494–1509 (1986).
1325 33. Bergstralh, D. T., Haack, T. & St Johnston, D. Epithelial polarity and spindle orientation: intersecting
1326 pathways. *Philos. Trans. R. Soc. B Biol. Sci.* **368**, 20130291 (2013).
1327 34. Buckley, C. E. & St Johnston, D. Apical–basal polarity and the control of epithelial form and function.
1328 *Nat. Rev. Mol. Cell Biol.* **23**, 559–577 (2022).
1329 35. Harris, T. J. C. & Peifer, M. Adherens junction-dependent and -independent steps in the
1330 establishment of epithelial cell polarity in Drosophila. *J. Cell Biol.* **167**, 135–47 (2004).
1331 36. Cao, J., Crest, J., Fasulo, B. & Sullivan, W. Cortical actin dynamics facilitate early-stage centrosome
1332 separation. *Curr. Biol.* **20**, 770–6 (2010).
1333 37. Rizzelli, F., Malabarba, M. G., Sigismund, S. & Mapelli, M. The crosstalk between microtubules, actin
1334 and membranes shapes cell division. *Open Biol.* **10**, 190314 (2020).
1335 38. McCartney, B. M. *et al.* Drosophila APC2 and Armadillo participate in tethering mitotic spindles to
1336 cortical actin. *Nat. Cell Biol.* **3**, 933–8 (2001).
1337 39. Rim, E. Y., Clevers, H. & Nusse, R. The Wnt Pathway: From Signaling Mechanisms to Synthetic
1338 Modulators. *Annu. Rev. Biochem.* **91**, 571–598 (2022).
1339 40. Mapelli, M. & Gonzalez, C. On the inscrutable role of Inscuteable: Structural basis and functional
1340 implications for the competitive binding of NuMA and Inscuteable to LGN. *Open Biol.* **2**, (2012).
1341 41. Ji, J.-Y., Haghnia, M., Trusty, C., Goldstein, L. S. B. & Schubiger, G. A Genetic Screen for Suppressors
1342 and Enhancers of the Drosophila Cdk1-Cyclin B Identifies Maternal Factors That Regulate
1343 Microtubule and Microfilament Stability. *Genetics* **162**, 1179–1195 (2002).
1344 42. Cadigan, K. M. & Nusse, R. Wnt signaling: a common theme in animal development. *Genes Dev.* **11**,
1345 3286–3305 (1997).
1346 43. Pires-daSilva, A. & Sommer, R. J. The evolution of signalling pathways in animal development. *Nat.*
1347 *Rev. Genet.* **4**, 39–49 (2003).
1348 44. Long, Y. C., Chin Tan, T. M., Takao, I. & Tang, B. L. The biochemistry and cell biology of aging:
1349 Metabolic regulation through mitochondrial signaling. *Am. J. Physiol. - Endocrinol. Metab.* **306**,
1350 (2014).
1351 45. Bitto, A., Wang, A. M., Bennett, C. F. & Kaeberlein, M. Biochemical genetic pathways that modulate
1352 aging in multiple species. *Cold Spring Harb. Perspect. Med.* **5**, 1–25 (2015).
1353 46. Hale, R. & Strutt, D. Conservation of Planar Polarity Pathway Function Across the Animal Kingdom.
1354 *Annu. Rev. Genet.* **49**, 529–551 (2015).
1355 47. Wright, B. A., Kvansakul, M., Schierwater, B. & Humbert, P. O. Cell polarity signalling at the birth of
1356 multicellularity: What can we learn from the first animals. *Front. Cell Dev. Biol.* **10**, 1–19 (2022).
1357 48. Schlacht, A., Herman, E. K., Klute, M. J., Field, M. C. & Dacks, J. B. Missing Pieces of an Ancient
1358 Puzzle: Evolution of the Eukaryotic Membrane-Trafficking System. *Cold Spring Harb. Perspect. Biol.*
1359 **6**, a016048–a016048 (2014).
1360 49. Harashima, H., Dissmeyer, N. & Schnittger, A. Cell cycle control across the eukaryotic kingdom.
1361 *Trends Cell Biol.* **23**, 345–356 (2013).
1362 50. Erickson, H. P. Evolution of the cytoskeleton. *BioEssays* **29**, 668–677 (2007).
1363 51. Wickstead, B. & Gull, K. The evolution of the cytoskeleton. *J. Cell Biol.* **194**, 513–525 (2011).
1364 52. Vazquez, J., Pauli, D. & Tissières, A. Transcriptional regulation in Drosophila during heat shock: a
1365 nuclear run-on analysis. *Chromosoma* **102**, 233–48 (1993).
1366 53. Leemans, R. *et al.* Quantitative transcript imaging in normal and heat-shocked Drosophila embryos

1367 by using high-density oligonucleotide arrays. *Proc. Natl. Acad. Sci.* **97**, 12138–43 (2000).
1368 54. Feder, M. E., Cartaño, N. V., Milos, L., Krebs, R. A. & Lindquist, S. L. Effect of engineering Hsp70 copy
1369 number on Hsp70 expression and tolerance of ecologically relevant heat shock in larvae and pupae
1370 of Drosophila melanogaster. *J. Exp. Biol.* **199**, 1837–44 (1996).
1371 55. Feder, M. E., Blair, N. & Figueras, H. Natural thermal stress and heat-shock protein expression in
1372 Drosophila larvae and pupae. *Funct. Ecol.* **11**, 90–100 (1997).
1373 56. Sørensen, J. G., Nielsen, M. M., Kruhøffer, M., Justesen, J. & Loeschcke, V. Full genome gene
1374 expression analysis of the heat stress response in Drosophila melanogaster. *Cell Stress Chaperones*
1375 **10**, 312–28 (2005).
1376 57. Lockwood, B. L., Julick, C. R. & Montooth, K. L. Maternal loading of a small heat shock protein
1377 increases embryo thermal tolerance in Drosophila melanogaster. *J. Exp. Biol.* **220**, 4492–4501
1378 (2017).
1379 58. Rutherford, S. L. & Lindquist, S. Hsp90 as a capacitor for morphological evolution. *Nature* **396**, 336–
1380 42 (1998).
1381 59. Sangster, T. A., Lindquist, S. & Queitsch, C. Under cover: causes, effects and implications of Hsp90-
1382 mediated genetic capacitance. *BioEssays* **26**, 348–62 (2004).
1383 60. Rudman, S. M. *et al.* Direct observation of adaptive tracking on ecological time scales in Drosophila.
1384 *Science (80-.).* **375**, (2022).
1385 61. Lynch, J. A., El-Sherif, E. & Brown, S. J. Comparisons of the embryonic development of Drosophila ,
1386 Nasonia , and Tribolium. *Wiley Interdiscip. Rev. Dev. Biol.* **1**, 16–39 (2012).
1387 62. Lemke, S., Kale, G. & Urbansky, S. Comparing gastrulation in flies: Links between cell biology and the
1388 evolution of embryonic morphogenesis. *Mech. Dev.* **164**, 103648 (2020).
1389 63. Raguso, R. A. Don't forget the flies: dipteran diversity and its consequences for floral ecology and
1390 evolution. *Appl. Entomol. Zool.* **55**, 1–7 (2020).
1391 64. Harvey, J. A., Heinen, R., Gols, R. & Thakur, M. P. Climate change-mediated temperature extremes
1392 and insects: From outbreaks to breakdowns. *Glob. Chang. Biol.* **26**, 6685–6701 (2020).
1393 65. Wagner, D. L., Grames, E. M., Forister, M. L., Berenbaum, M. R. & Stopak, D. Insect decline in the
1394 Anthropocene: Death by a thousand cuts. *Proc. Natl. Acad. Sci.* **118**, 1–10 (2021).
1395 66. Condamine, F. L., Clapham, M. E. & Kergoat, G. J. Global patterns of insect diversification: towards a
1396 reconciliation of fossil and molecular evidence? *Sci. Rep.* **6**, 19208 (2016).
1397 67. Wiegmann, B. M. B. Episodic radiations in the fly tree of life. *Proc. …* **108**, 5690–5695 (2011).
1398 68. Clapham, M. E. & Karr, J. A. Environmental and biotic controls on the evolutionary history of insect
1399 body size. *Proc. Natl. Acad. Sci.* **109**, 10927–10930 (2012).
1400 69. Wang, B., Xu, C. & Jarzembowski, E. A. Ecological radiations of insects in the Mesozoic. *Trends Ecol.*
1401 *Evol.* **37**, 529–540 (2022).
1402 70. Chown, S. L. & Gaston, K. J. Body size variation in insects: a macroecological perspective. *Biol. Rev.*
1403 **85**, 139–169 (2010).
1404 71. Bogovic, J. A., Hanslovsky, P., Wong, A. & Saalfeld, S. Robust registration of calcium images by
1405 learned contrast synthesis. in *2016 IEEE 13th International Symposium on Biomedical Imaging (ISBI)*
1406 vols 2016-June 1123–1126 (IEEE, 2016).
1407 72. Pietzsch, T., Saalfeld, S., Preibisch, S. & Tomancak, P. BigDataViewer: visualization and processing for
1408 large image data sets. *Nat. Methods* **12**, 481–3 (2015).
1409 73. Preibisch, S., Saalfeld, S. & Tomancak, P. Globally optimal stitching of tiled 3D microscopic image
1410 acquisitions. *Bioinformatics* **25**, 1463–1465 (2009).
1411 74. Ollion, J., Cochennec, J., Loll, F., Escudé, C. & Boudier, T. TANGO: a generic tool for high-throughput
1412 3D image analysis for studying nuclear organization. *Bioinformatics* **29**, 1840–1 (2013).
1413 75. Herbert, S. *et al.* LocalZProjector and DeProj: a toolbox for local 2D projection and accurate
1414 morphometrics of large 3D microscopy images. *BMC Biol.* **19**, 136 (2021).

1415 76. Telley, I. A., Gáspár, I., Ephrussi, A. & Surrey, T. Aster migration determines the length scale of
1416 nuclear separation in the Drosophila syncytial embryo. *J. Cell Biol.* **197**, 887–895 (2012).
1417 77. Oakeshott, J. G., McKechnie, S. W. & Chambers, G. K. Population genetics of the metabolically
1418 related Adh, Gpdh and Tpi polymorphisms in Drosophila melanogaster I. Geographic variation in
1419 Gpdh and Tpi allele frequencies in different continents. *Genetica* **63**, 21–29 (1984).
1420 78. McColl, G. & McKechnie, S. W. The Drosophila heat shock hsr-omega gene: An allele frequency cline
1421 detected by quantitative PCR. *Mol. Biol. Evol.* **16**, 1568–1574 (1999).
1422 79. Bettencourt, B. R., Kim, I., Hoffmann, A. A. & Feder, M. E. Response to natural and laboratory
1423 selection at the Drosophila hsp70 genes. *Evolution (N. Y).* **56**, 1796–1801 (2002).
1424 80. Frydenberg, J., Hoffmann, A. A. & Loeschcke, V. DNA sequence variation and latitudinal associations
1425 in hsp23, hsp26 and hsp27 from natural populations of Drosophila melanogaster. *Mol. Ecol.* **12**,
1426 2025–2032 (2003).
1427 81. Umina, P. A., Weeks, A. R., Kearney, M. R., McKechnie, S. W. & Hoffmann, A. A. Evolution: A rapid
1428 shift in a classic clinal pattern in Drosophila reflecting climate change. *Science (80-.).* **308**, 691–693
1429 (2005).
1430 82. Sawyer, L. A. *et al.* The period gene Thr-Gly polymorphism in Australian and African Drosophila
1431 melanogaster populations: Implications for selection. *Genetics* **174**, 465–480 (2006).
1432 83. Weeks, A. R., Mckechnie, S. W. & Hoffmann, A. A. In search of clinal variation in the period and clock
1433 timing genes in Australian Drosophila melanogaster populations. *J. Evol. Biol.* **19**, 551–557 (2006).
1434 84. Rand, D. M., Weinreich, D. M., Lerman, D., Folk, D. & Gilchrist, G. W. Three selections are better
1435 than one: Clinal variation of thermal QTL from independent selection experiments in drosophila.
1436 *Evolution (N. Y).* **64**, 2921–2934 (2010).
1437 85. Kolaczkowski, B., Kern, A. D., Holloway, A. K. & Begun, D. J. Genomic differentiation between
1438 temperate and tropical Australian populations of Drosophila melanogaster. *Genetics* **187**, 245–260
1439 (2011).
1440 86. Paaby, A. B., Bergland, A. O., Behrman, E. L. & Schmidt, P. S. A highly pleiotropic amino acid
1441 polymorphism in the Drosophila insulin receptor contributes to life-history adaptation. *Evolution* **68**,
1442 3395–409 (2014).
1443 87. Vigue, C. L. & Johnson, F. M. Isozyme Variability in Species of the Genus Drosophila. VI. Frequency-
1444 Property-Environment Relationships of Allelic Alcohol Dehydrogenases in D. melanogaster. *Biochem.*
1445 *Genet.* **9**, 213–227 (1973).
1446 88. Berry, A. & Kreitman, M. Molecular analysis of an allozyme cline: alcohol dehydrogenase in
1447 Drosophila melanogaster on the east coast of North America. *Genetics* **134**, 869–93 (1993).
1448 89. Duvernell, D. D. & Eanes, W. F. Contrasting molecular population genetics of four hexokinases in
1449 Drosophila melanogaster, D. simulans and D. yakuba. *Genetics* **156**, 1191–1201 (2000).
1450 90. Schmidt, P. S., Duvernell, D. D. & Eanes, W. F. Adaptive evolution of a candidate gene for aging in
1451 Drosophila. *Proc. Natl. Acad. Sci.* **97**, 10861–10865 (2000).
1452 91. Verrelli, B. C. & Eanes, W. F. Clinal variation for amino acid polymorphisms at the Pgm locus in
1453 Drosophila melanogaster. *Genetics* **157**, 1649–1663 (2001).
1454 92. Duvernell, D. D., Schmidt, P. S. & Eanes, W. F. Clines and adaptive evolution in the methuselah gene
1455 region in Drosophila melanogaster. *Mol. Ecol.* **12**, 1277–1285 (2003).
1456 93. Sezgin, E. *et al.* Single-locus latitudinal clines and their relationship to temperate adaptation in
1457 metabolic genes and derived alleles in Drosophila melanogaster. *Genetics* **168**, 923–931 (2004).
1458 94. Schmidt, P. S. & Paaby, A. B. Reproductive diapause and life-history clines in North American
1459 populations of Drosophila melanogaster. *Evolution (N. Y).* **62**, 1204–1215 (2008).
1460 95. Fabian, D. K. *et al.* Genome-wide patterns of latitudinal differentiation among populations of
1461 Drosophila melanogaster from North America. *Mol. Ecol.* **21**, 4748–4769 (2012).
1462 96. Machado, H. E. *et al.* Comparative population genomics of latitudinal variation in Drosophila

1463 simulans and Drosophila melanogaster. *Mol. Ecol.* **25**, 723–40 (2016).
1464 97. Costa, R., Peixoto, A. A., Barbujani, G. & Kyriacou, C. P. A latitudinal cline in a Drosophila clock gene.
1465 *Proc. R. Soc. London* 43–49 (1992).
1466 98. Kapun, M. *et al.* Genomic Analysis of European Drosophila melanogaster Populations Reveals
1467 Longitudinal Structure, Continent-Wide Selection, and Previously Unknown DNA Viruses. *Mol. Biol.*
1468 *Evol.* **37**, 2661–2678 (2020).
1469 99. Graveley, B. R. *et al.* The developmental transcriptome of Drosophila melanogaster. *Nature* **471**,
1470 473–479 (2011).
1471

Figure 1

Increased embryonic lethality at elevated temperature

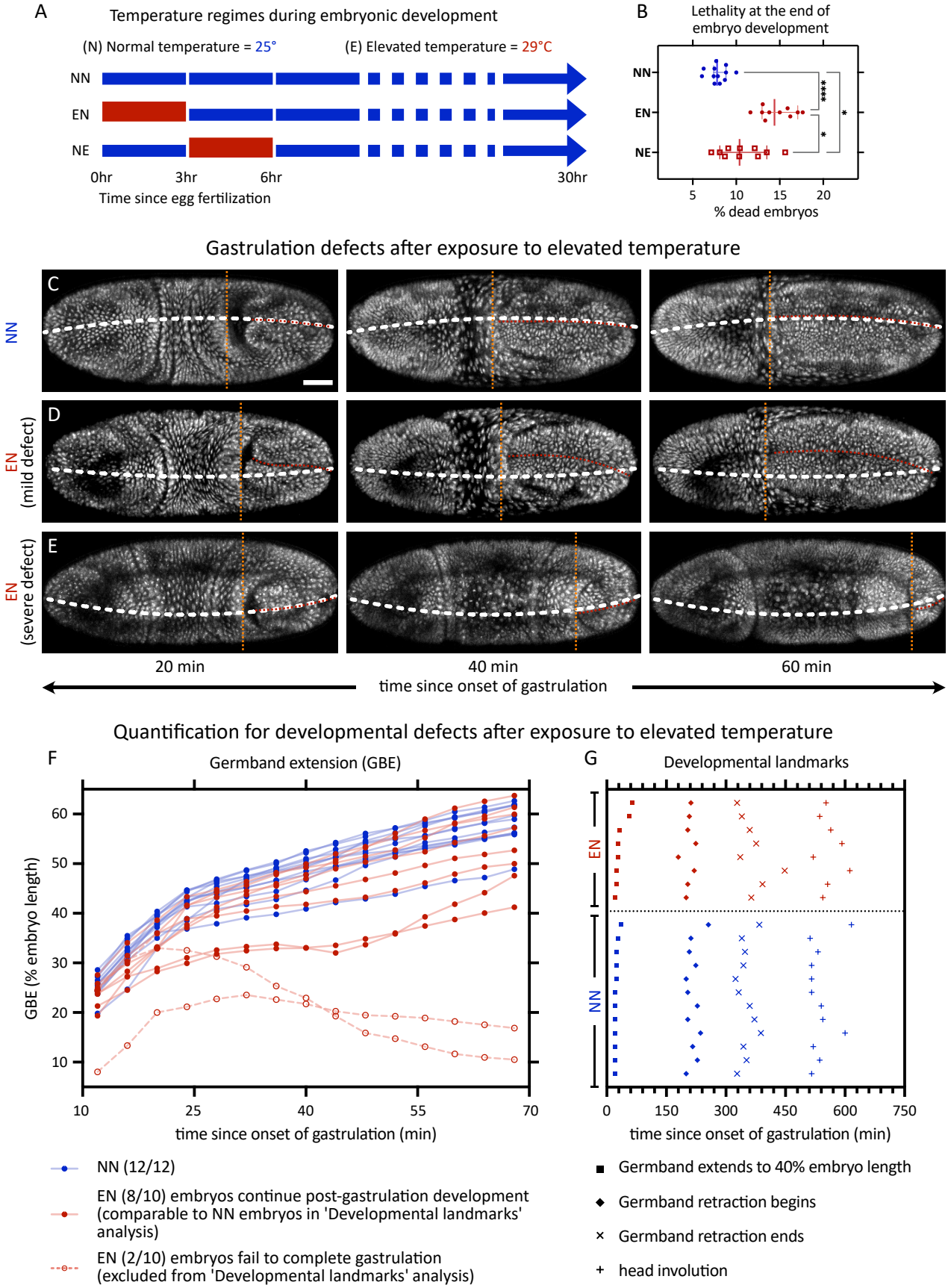

Figure 2

The distribution of blastoderm holes is not bilaterally symmetrical

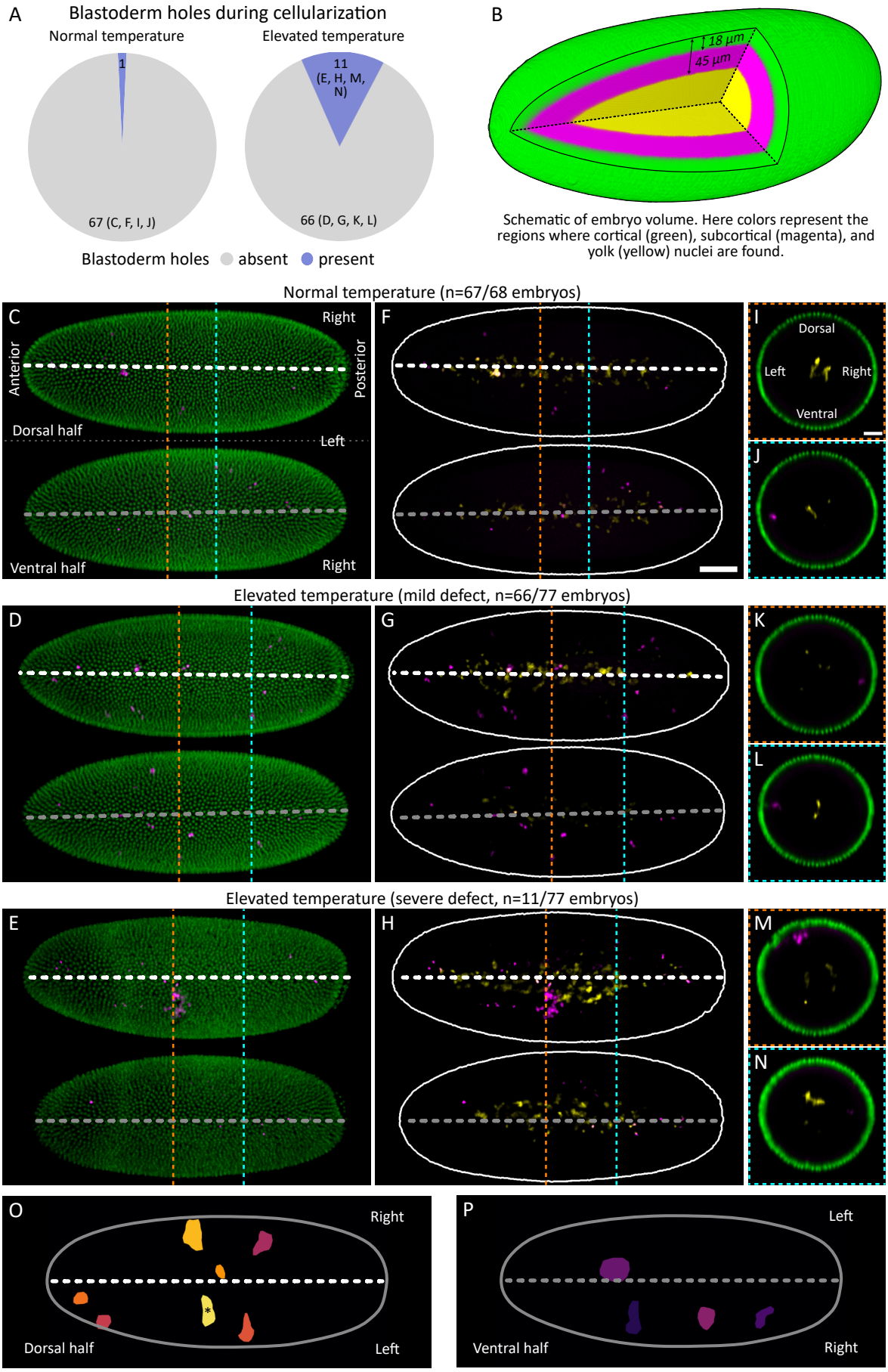

Figure 3

Nuclear expulsion at elevated temperature

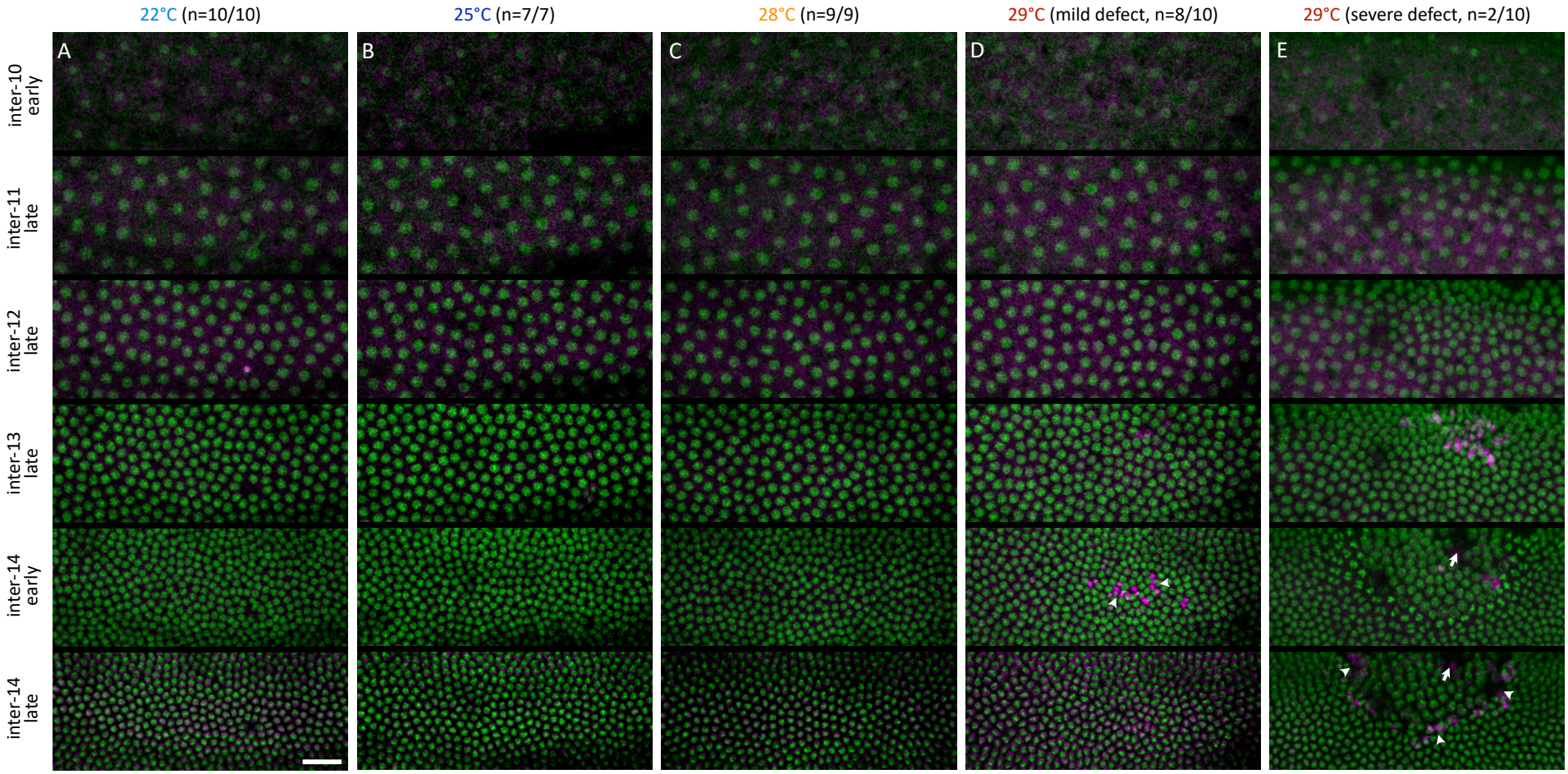

Cortical and Subcortical (lost) nuclei

Figure 4

Isolated nuclear expulsion

A

out-of-plane divisions (Example from embryo at 25°C)

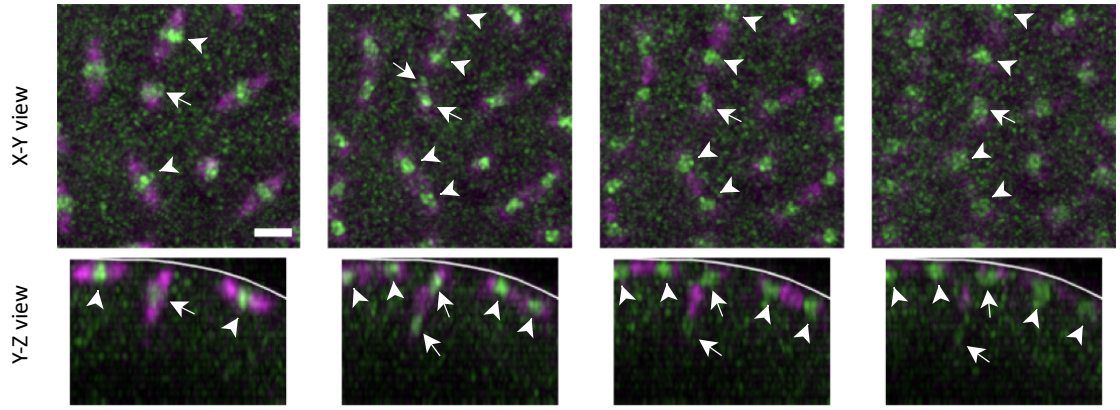

Histone-RFP Jupiter-GFP

B

in-plane divisions (Example from embryo at 25°C)

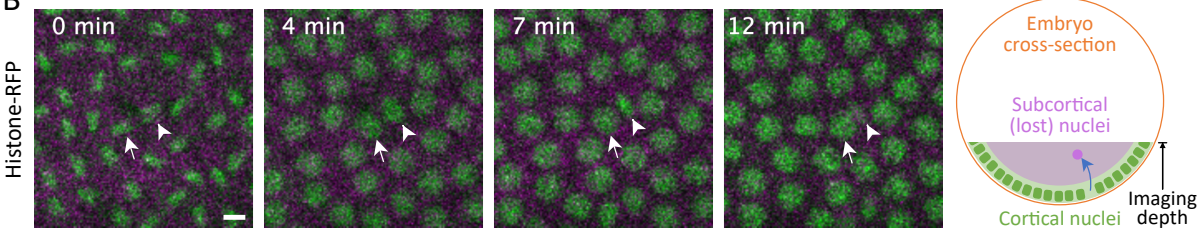

Cortical and Subcortical (lost) nuclei

C

out-of-plane divisions during mitosis-10

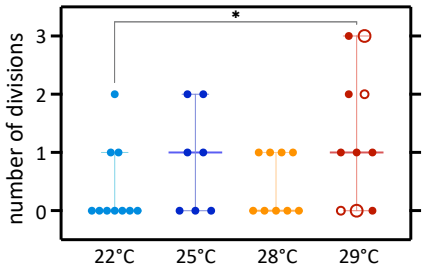

D

number of isolated nuclear expulsions during interphase 14

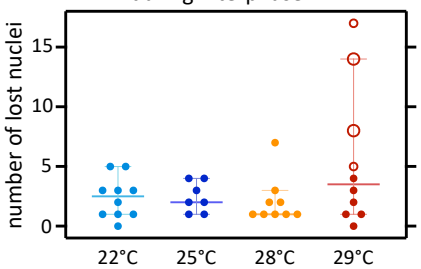

Pairwise nuclear expulsion after in-plane divisions due to Mitotic failure

(Example from embryo at 29°C)

E

Histone-RFP

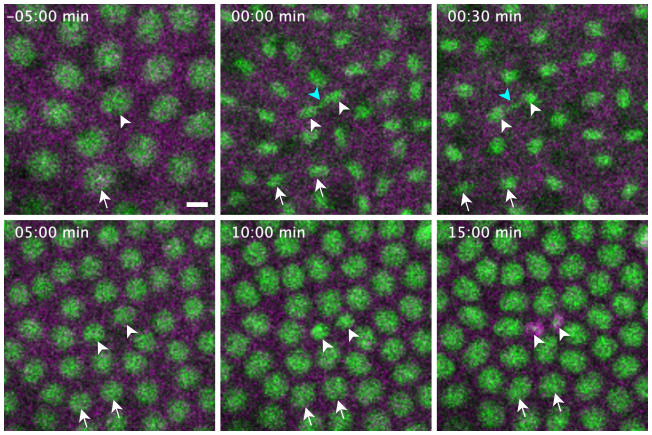

Cortical and Subcortical (lost) nuclei

F

number of mitotic failures causing nuclear expulsions during interphase 14

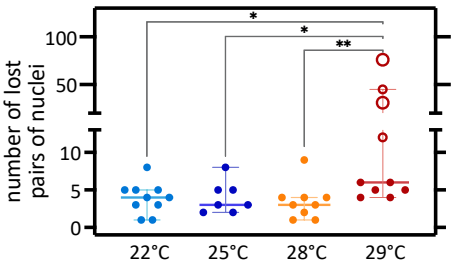

G

Mitotic failures increase at elevated temperature

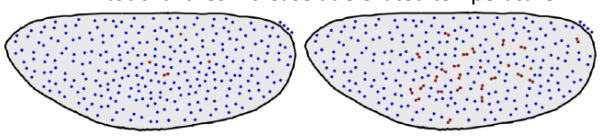

Normal temperature Elevated temperature

- Normal mitosis
- Mitotic failure and pairwise loss of nuclei

Figure 5

Nuclear group-center drift and deviations in x-y plane

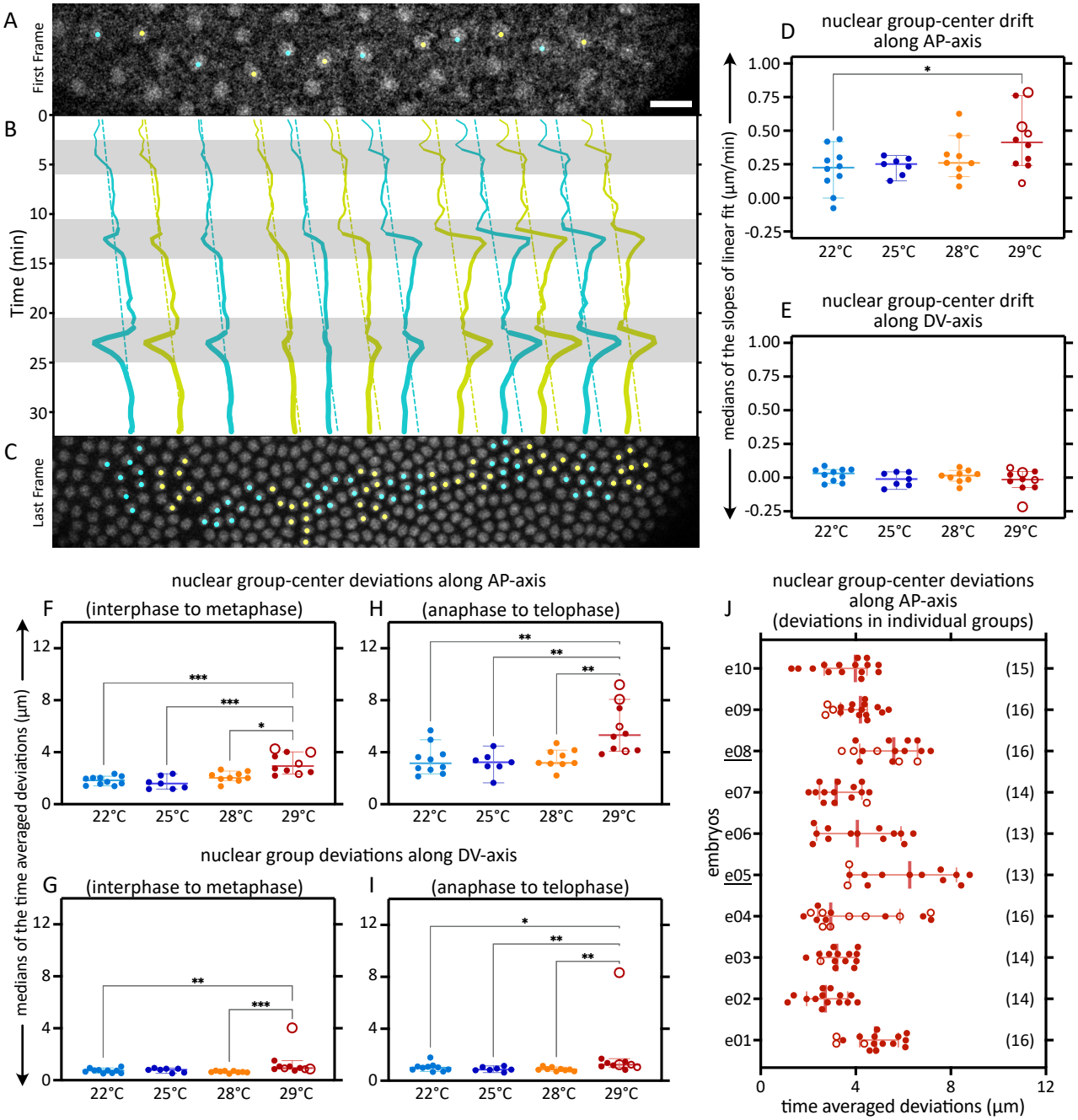

Figure 6

Increased nuclear crowding at elevated temperature

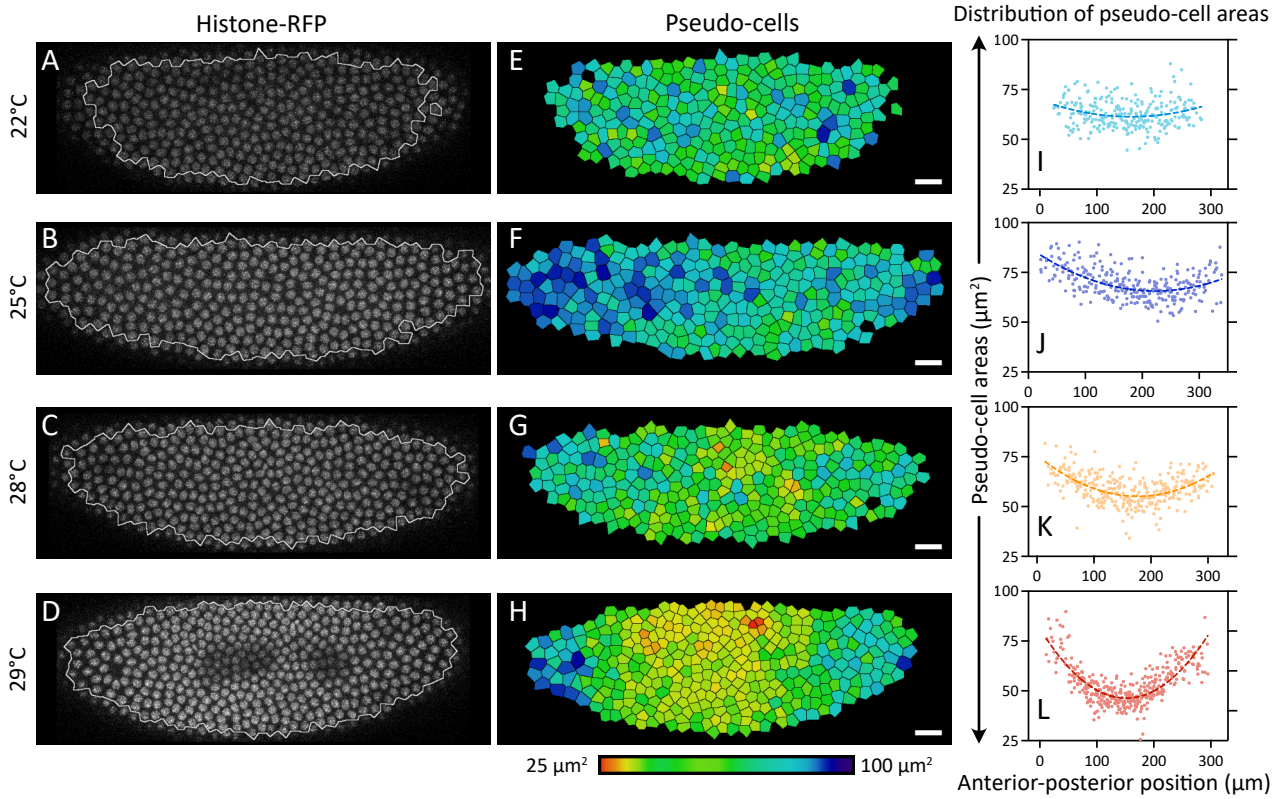

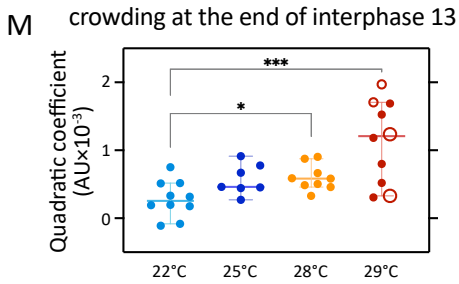

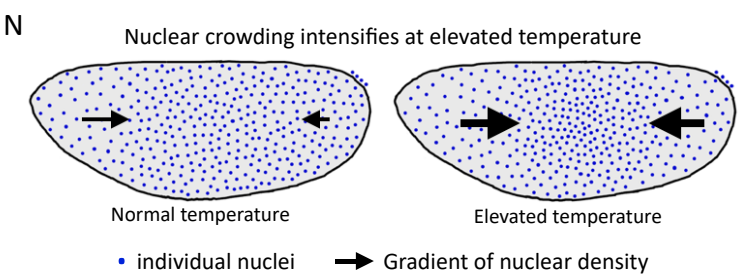

Asynchrony in the phases of nuclear division cycles at elevated temperature

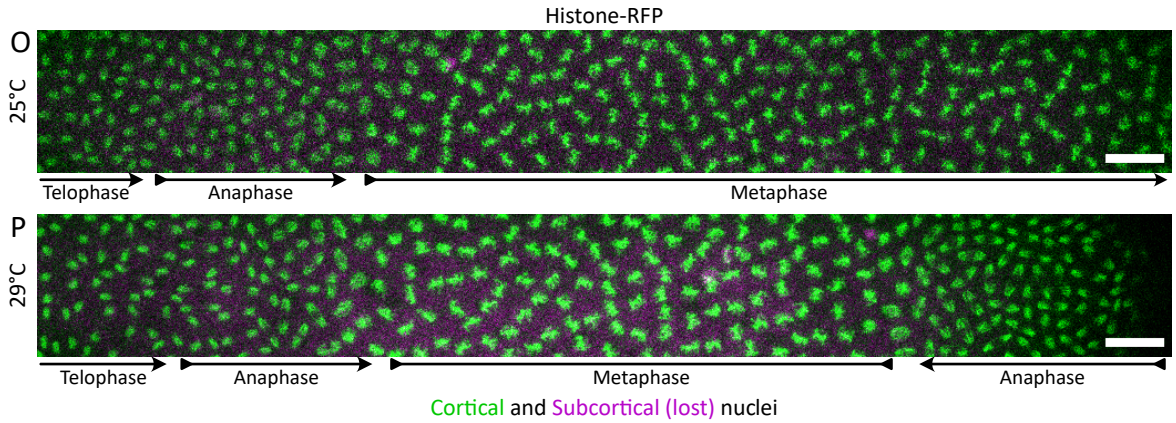

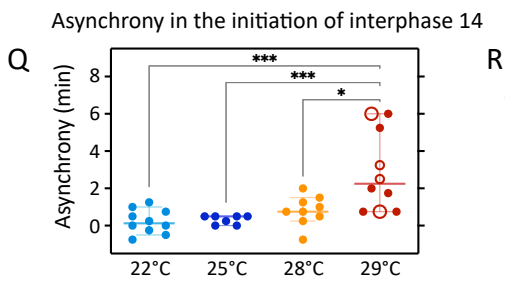

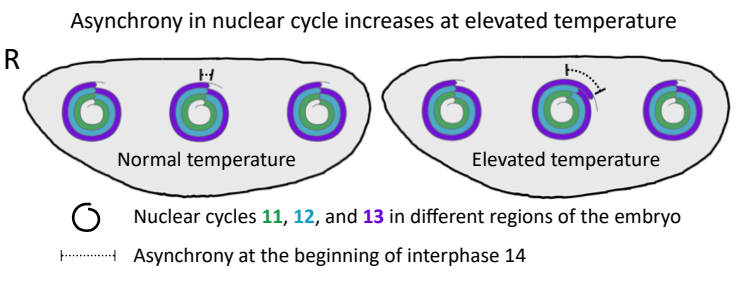

Figure 7 combinatorial effects of nuclear crowding and nuclear cycle asynchrony on distribution of mitotic failures at elevated temperature

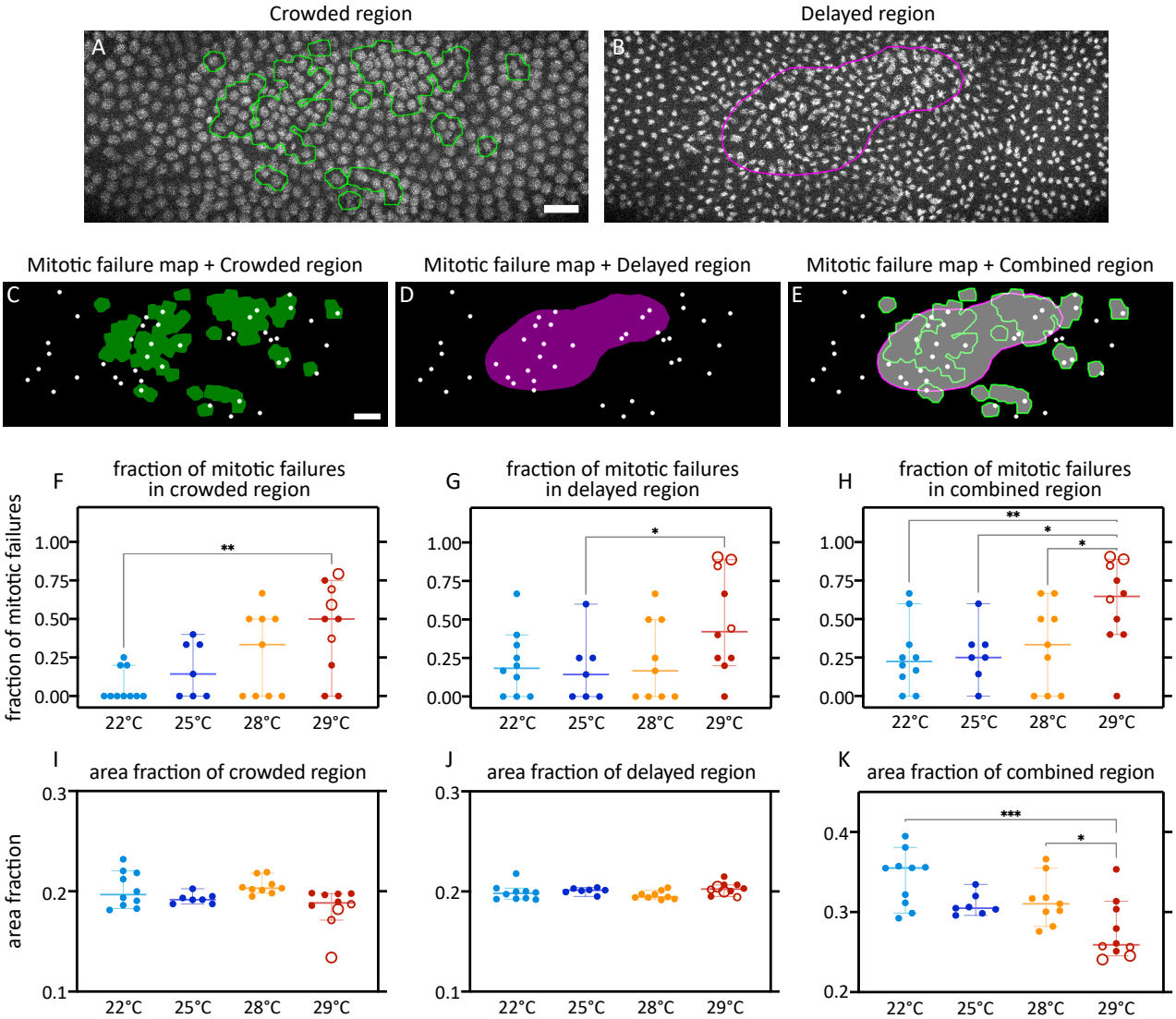

Figure 8

DNA damage response after mitotic failures at elevated temperature

A

Stem-Loop Binding Protein (SLBP) mislocalization as a DNA damage reporter

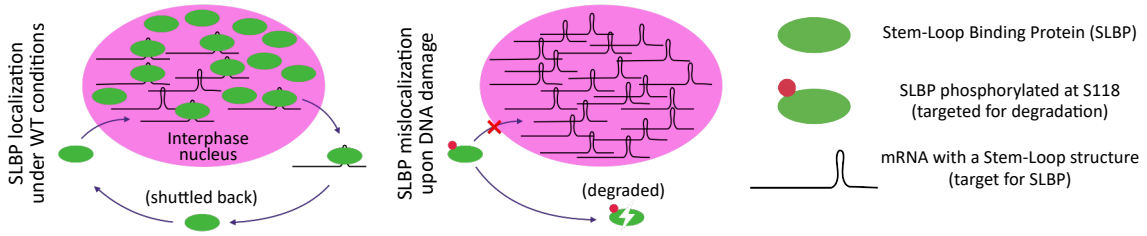

B

Nuclei with DNA damage are mitotically arrested

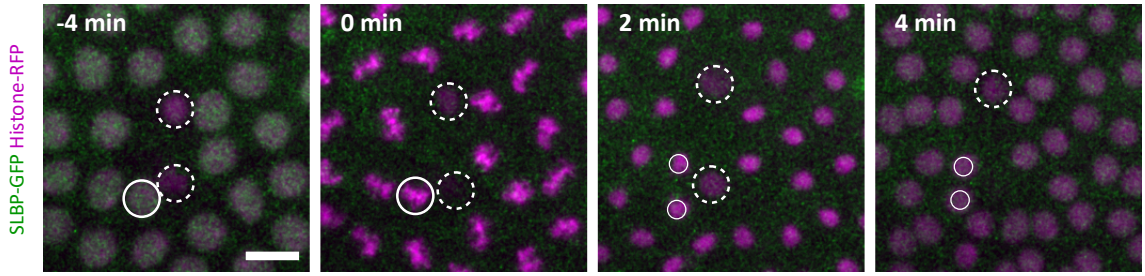

Mitotic failure leads to DNA damage response

C

Wild-type SLBP

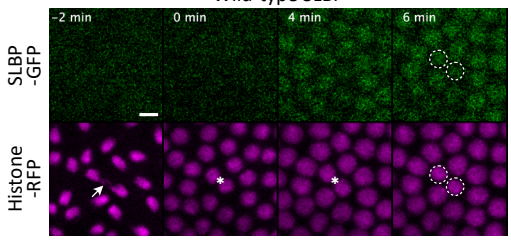

D

DNA damage insensitive SLBP

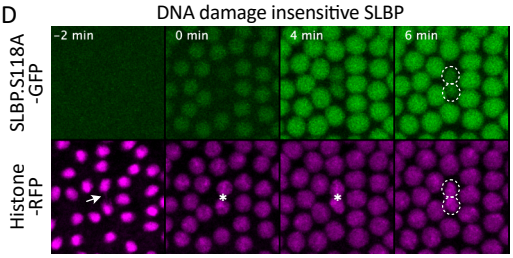

E

Nuclear Localization Signal (NLS)

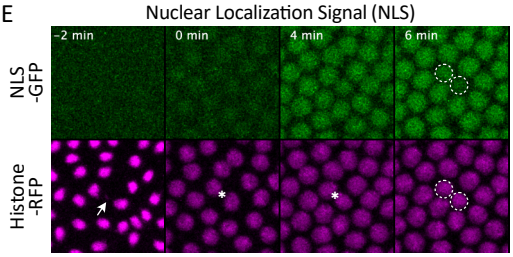

(representative embryos at 29°C)

nuclear recruitment kinetics

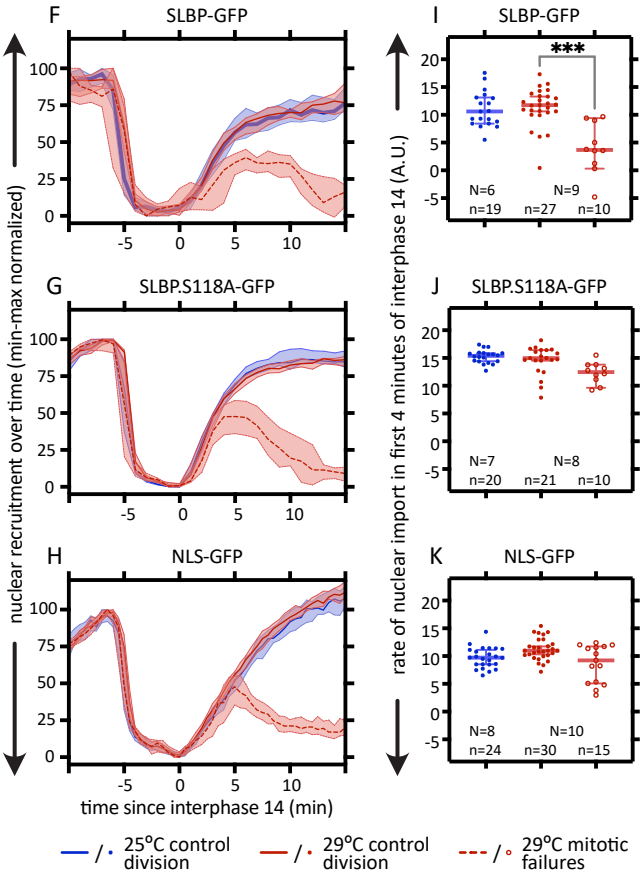

Figure 9

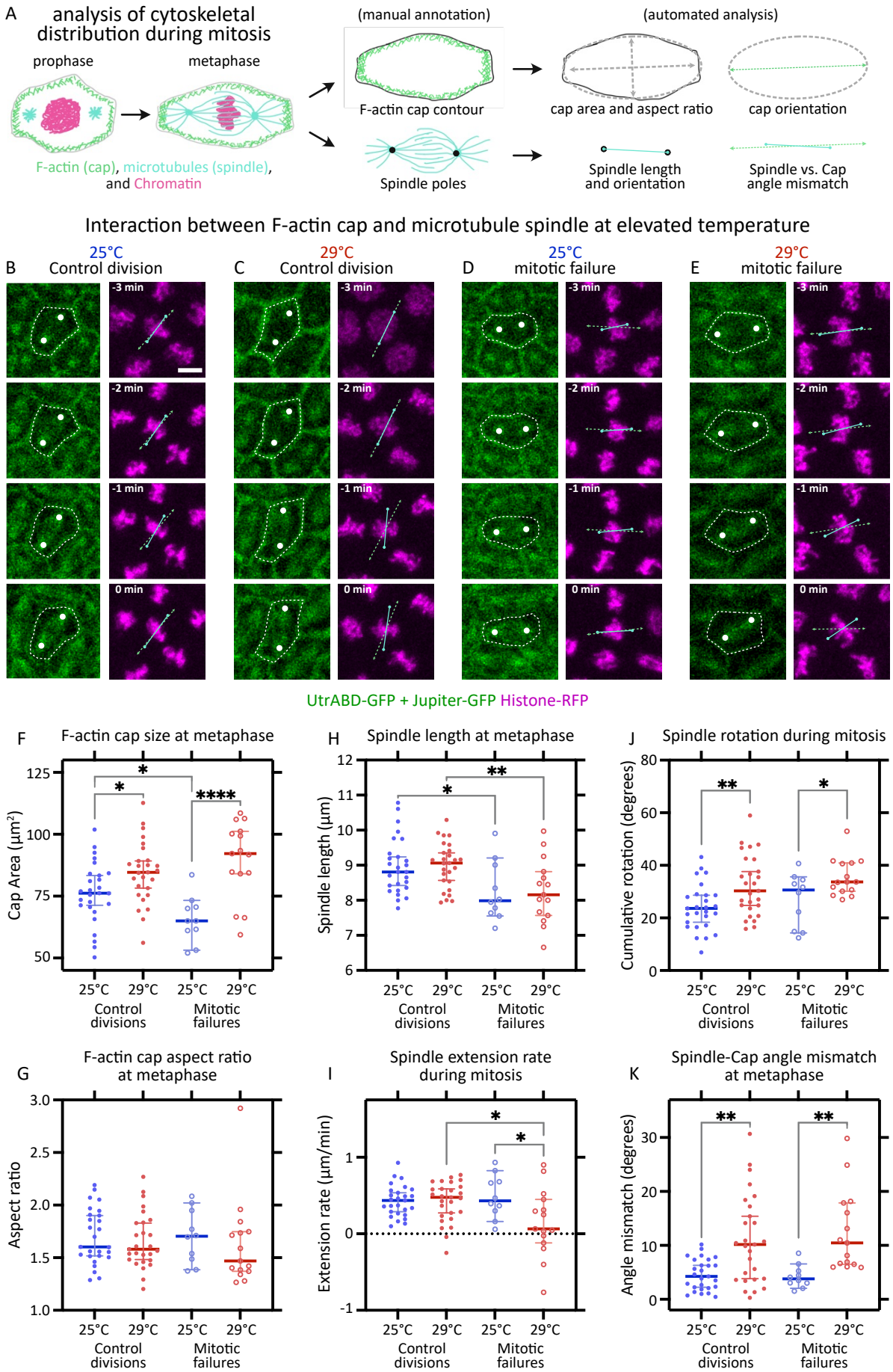
A
analysis of cytoskeletal distribution during mitosis
prophase
metaphase
F-actin (cap), microtubules (spindle), and Chromatin
(manual annotation)
(automated analysis)
F-actin cap contour
cap area and aspect ratio
cap orientation
Spindle poles
Spindle length and orientation
Spindle vs. Cap angle mismatch
Interaction between F-actin cap and microtubule spindle at elevated temperature
B 25°C Control division
C 29°C Control division
D 25°C mitotic failure
E 29°C mitotic failure
-3 min
-2 min
-1 min
0 min
UtrABD-GFP + Jupiter-GFP Histone-RFP
F F-actin cap size at metaphase
Cap Area (µm²)
H Spindle length at metaphase
Spindle length (µm)
J Spindle rotation during mitosis
Cumulative rotation (degrees)
G F-actin cap aspect ratio at metaphase
Aspect ratio
I Spindle extension rate during mitosis
Extension rate (µm/min)
K Spindle-Cap angle mismatch at metaphase
Angle mismatch (degrees)
25°C 29°C 25°C 29°C
Control divisions
Mitotic failures

Figure 10

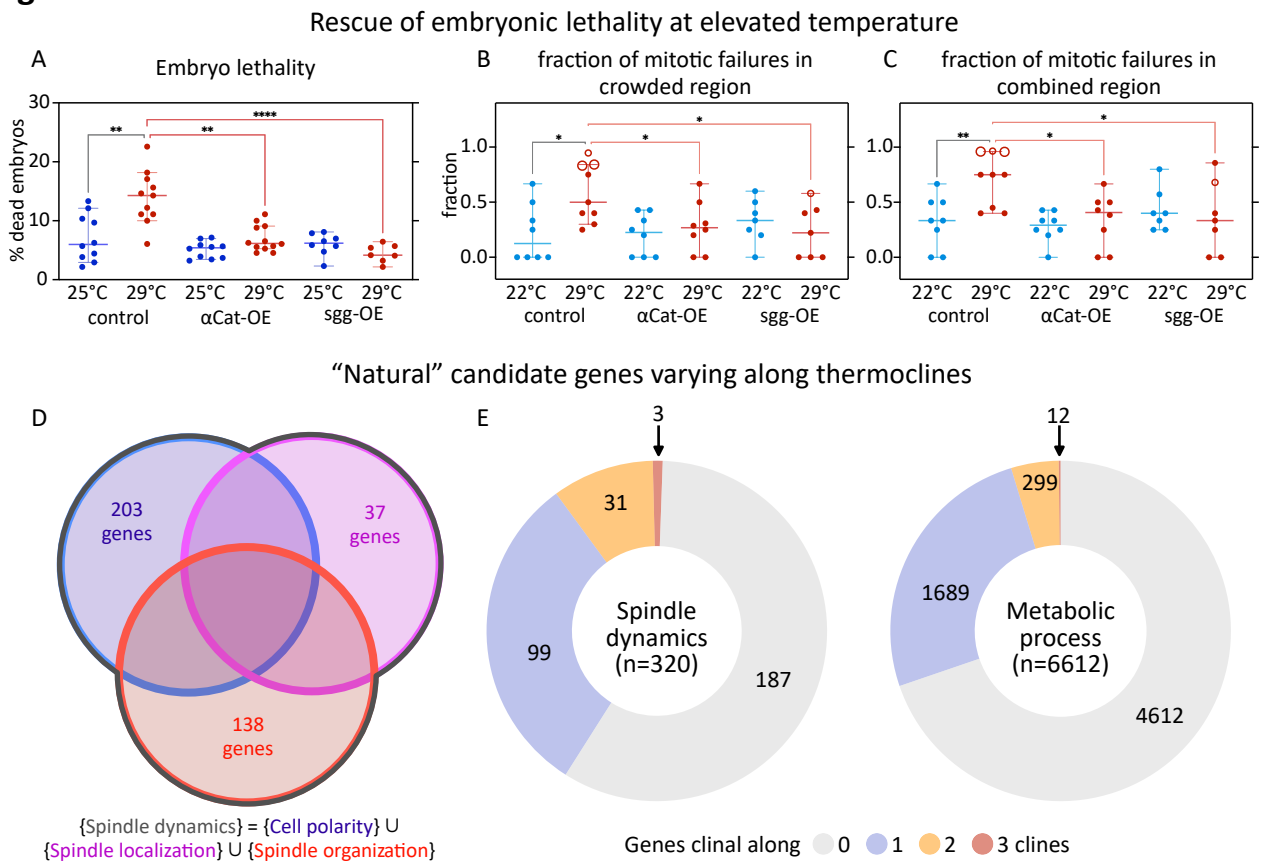
Rescue of embryonic lethality at elevated temperature
A
Embryo lethality
% dead embryos
30
20
10
0
**
**
****
25°C 29°C 25°C 29°C 25°C 29°C
control αCat-OE sgg-OE
B
fraction of mitotic failures in crowded region
fraction
1.0
0.5
0.0
*
*
*
22°C 29°C 22°C 29°C 22°C 29°C
control αCat-OE sgg-OE
C
fraction of mitotic failures in combined region
1.0
0.5
0.0
**
*
*
22°C 29°C 22°C 29°C 22°C 29°C
control αCat-OE sgg-OE
"Natural" candidate genes varying along thermoclines
D
203 genes
37 genes
138 genes
{Spindle dynamics} = {Cell polarity} ∪ {Spindle localization} ∪ {Spindle organization}
E
3
31
99
Spindle dynamics (n=320)
187
12
299
1689
Metabolic process (n=6612)
4612
Genes clinal along 0 1 2 3 clines

Figure S1

Blastoderm holes at elevated temperature

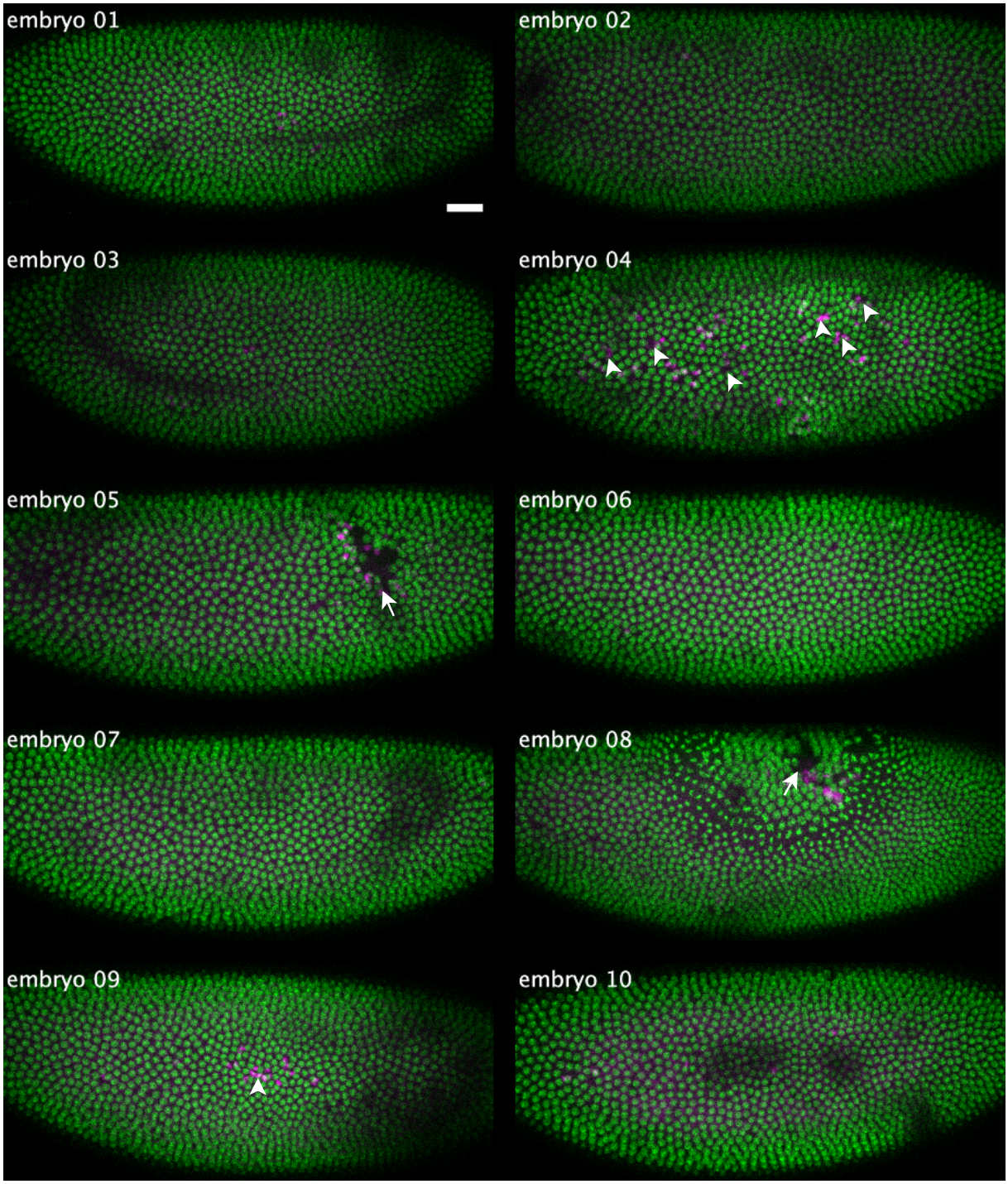

Figure S2

Nuclear expulsion is a passive process

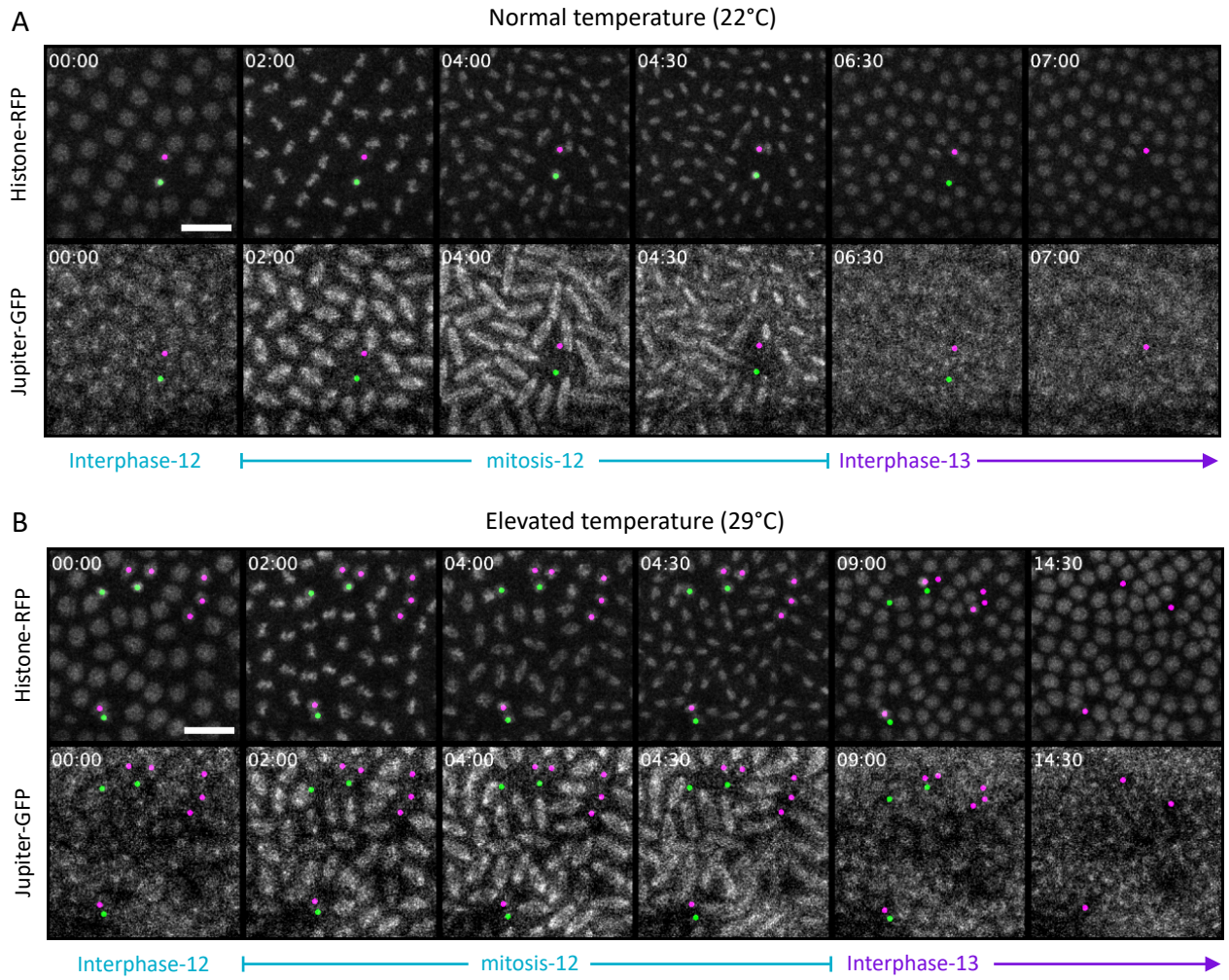

Figure S3

Nuclear movement along z axis at elevated temperature

A Normal temperature (22°C)

B Elevated temperature (29°C)

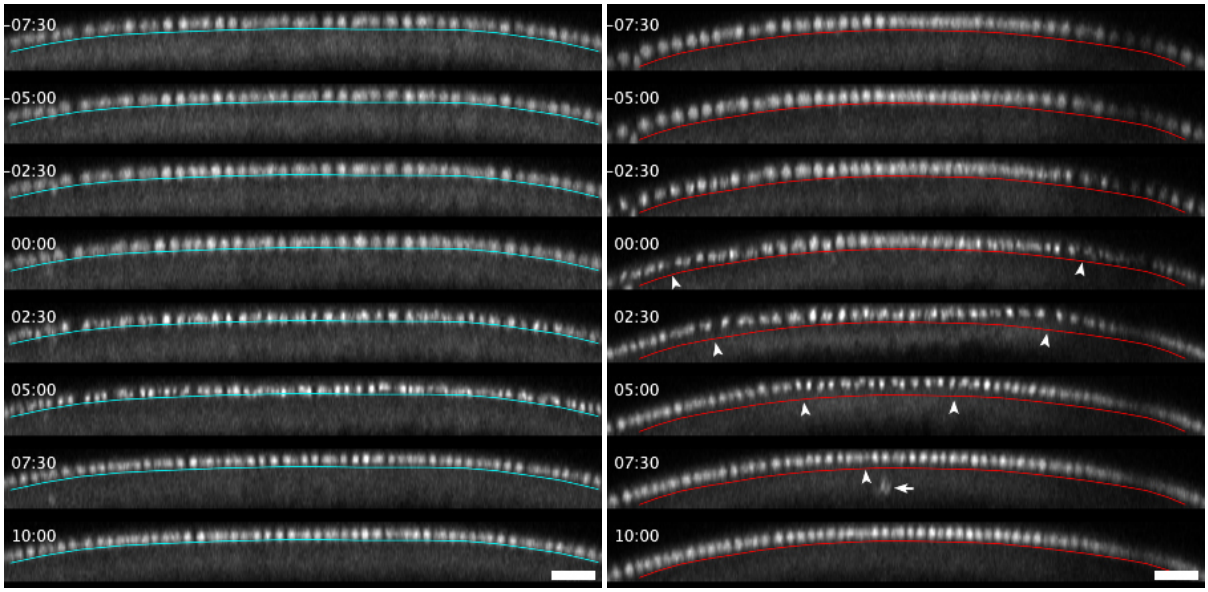

Figure S4

Asynchrony in the phases of nuclear division cycles at elevated temperature

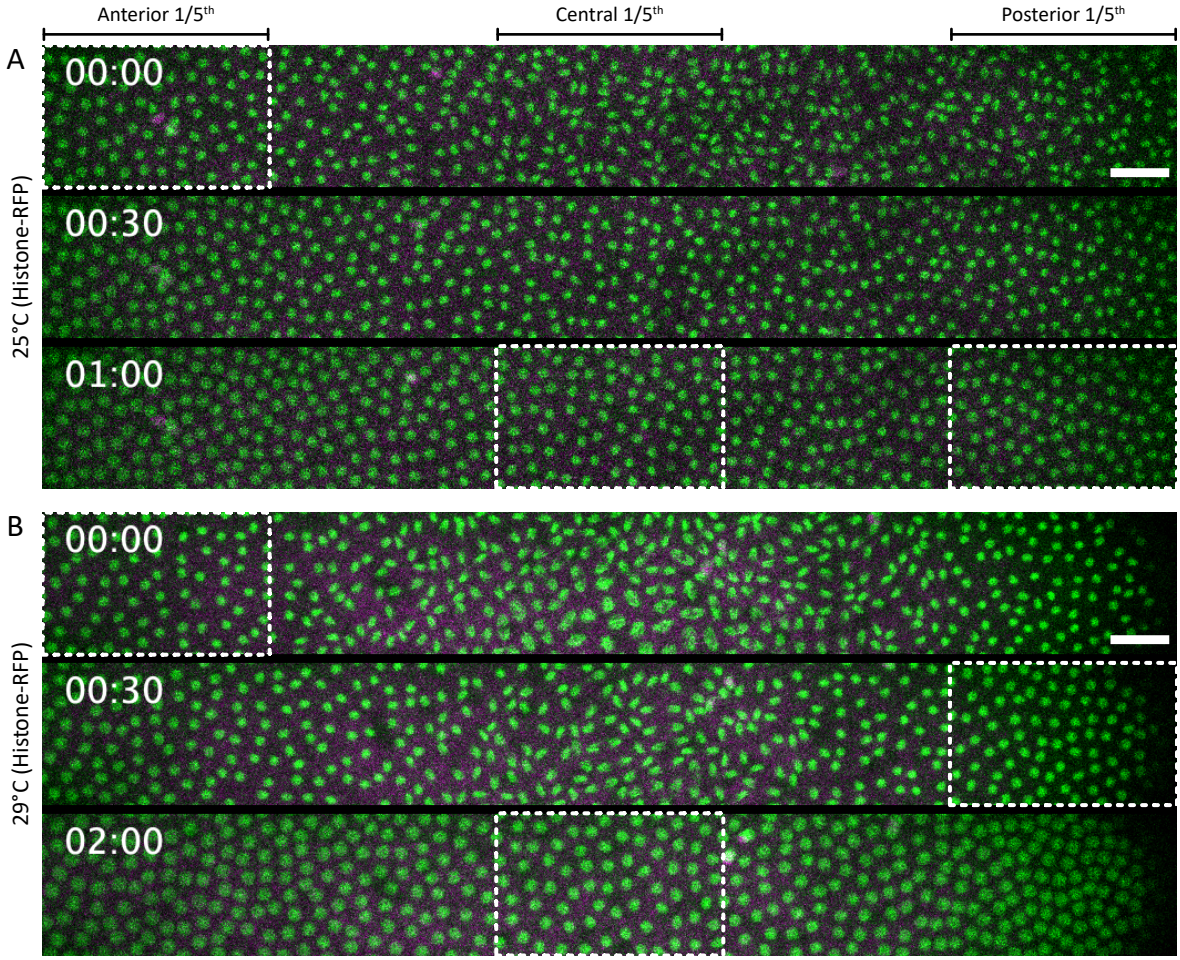

Cortical and Subcortical (lost) nuclei

Figure S5

Rescue of embryonic lethality at elevated temperature

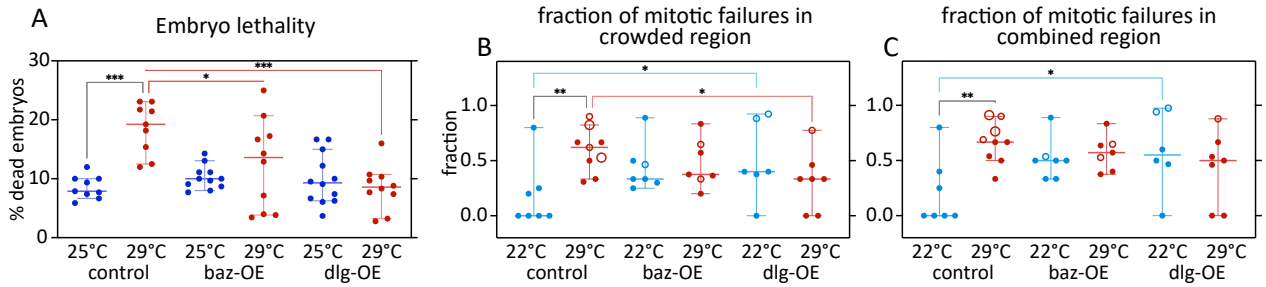

Figure S6

Empty F-actin caps at elevated temperature

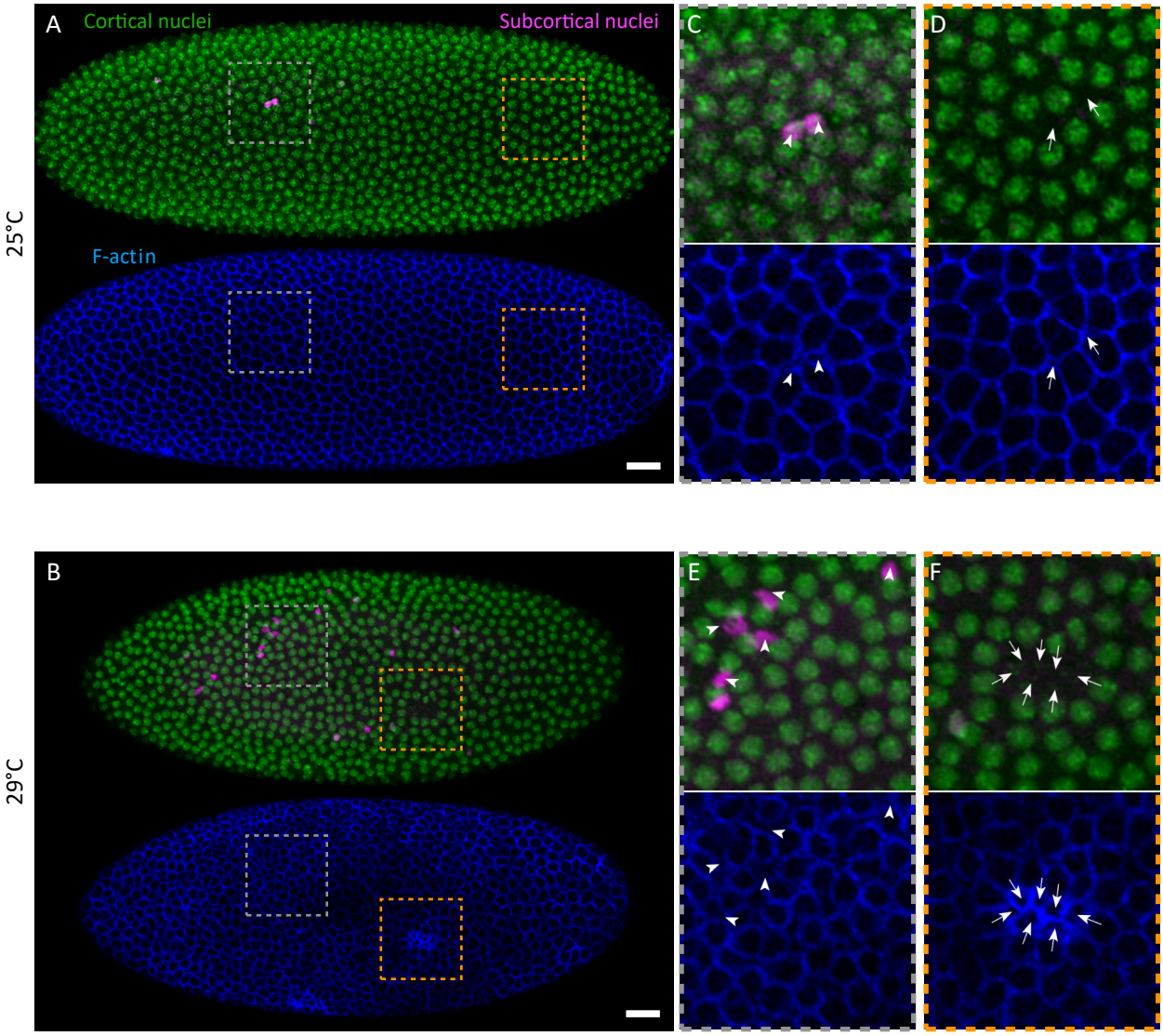

Figure S7
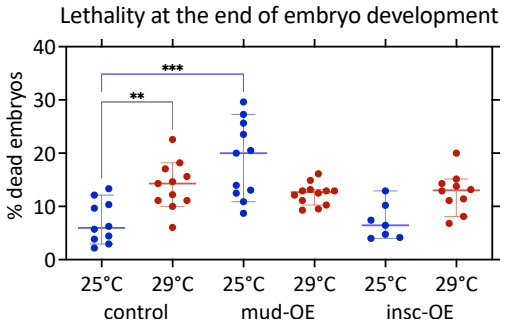
Rescue of embryonic lethality at elevated temperature